

Development of a Large-Eddy Simulation model for flows over urban areas with application to the TU Delft campus

by

Shenghao Zhang

to obtain the degree of Master of Science
at the Delft University of Technology,
to be defended publicly on Tuesday June 27, 2023 at 13:30.

Student number: 5473322
Project duration: February, 2023 - December, 2023
Thesis committee: Dr. Ir. Wim-Paul Breugem (supervisor)
Dr. Pedro Costa (daily supervisor)
Dr. Akshay Patil (advisor)
Dr. Stephan de Roode (independent member)

An electronic version of this thesis is available at <http://repository.tudelft.nl/>.

Abstract

Urban microclimate significantly affects people's experiences and activities in urban environments by a series of phenomena, among which urban flow is an important factor to be considered. Computational Fluid Dynamics (CFD) method has become a popular tool for studying urban airflow because of its low cost compared with experiment methods. However, flows over urban areas exhibit turbulence nature of being three-dimensional, unsteady, and multi-scale. Additionally, the large computational domain that should be covered and the inherent inhomogeneity of the urban structures make it challenging to do full-scale modelings. Large Eddy Simulation (LES), with the development of computing power, becomes a promising tool to study such flows.

In the campus of Delft University of Technology (TU Delft), a crossroad near the EWI building (the main building of Faculty of Electrical Engineering, Mathematics and Computer Science) is constantly complained for its strong wind. This research tackles such problem using LES, and takes TU Delft campus area itself as case study. The development of this research is composed of three stages.

In the first stage, Vreman eddy viscosity model is implemented into Canonical Navier-Stokes (CaNS), a massively-parallel Navier Stokes solver developed by Costa, (2018). Based on a structured three-dimensional Cartesian grid, the subgrid scale (SGS) eddy viscosity model is inserted into the Navier-Stokes equation by adding an extra diffusion term. The inserted diffusion term is discretized with second-order difference scheme along with interpolation of the velocity field due to the staggered grid arrangement. The implementation is validated with a turbulent channel flow with friction Reynolds number $Re_\tau = 360$. The good agreement is found and the discrepancy is small.

In the second stage, the solver employs a direct-forcing Immersed Boundary Method (IBM), and is further validated with the flow over periodic cube arrays. Signed-Distance Field (SDF), as a convenient tool, is generated and functions as read-in data for IBM. The IBM processes the effect of the boundary as an added force on the fluid points at the interface. The stair-step approach approximates the structure boundary with the cuboid cells faces. The results match well with the wind tunnel test data from Castro et al., (2006) and a previous LES study by Tomas et al., (2016).

In the last stage, the validated solver is applied to a scaled-down TU Delft campus model. The simulation setup is designed by considering the achievability of a possible future wind tunnel measurement. Three grids are used for a grid convergence analysis by comparing the total IBM force, mean velocity, and Reynolds stress at certain locations. The flow converges with the finest grid with grid number $N_x \times N_y \times N_z = 960 \times 880 \times 240$. Around the EWI building, a high speed region is found at the crossroad location. Behind the building, a wake area is observed and a clear shear layer is on the top of the building.

Contents

Abstract	iii
1 Introduction	1
2 Literature review	3
2.1 Urban Microclimate	3
2.2 Pedestrian-level Wind	4
2.3 Wind Comfort Criteria	4
2.4 CFD Methods	5
2.4.1 RANS	5
2.4.2 LES	6
2.4.3 DNS	6
2.4.4 Immersed Boundary Method	6
2.5 Focus of the Present Studies	7
2.5.1 Flow Around a Single Building	7
2.5.2 Street Canyons	8
2.5.3 Actual Urban Areas	11
2.6 Research Outline	12
3 Numerical Methods	13
3.1 Introduction	13
3.2 Governing equations	13
3.3 Subgrid Scale Model	14
3.4 Discretization	15
3.4.1 Velocity Gradient	15
3.4.2 Advection Term	17
3.4.3 Pressure Term	19
3.4.4 Diffusion Term	19
3.5 Signed Distance Field	21
3.6 Immersed Boundary Method	22
4 Channel Flow Validation	25
4.1 DNS Validation	25
4.2 LES Validation	26
4.2.1 Flow Setup	26
4.3 Results	27
5 Flow Over Cube Array Validation	33
5.1 Introduction	33
5.2 Flow Setup	33
5.3 Results	35
6 Flow Over Delft Campus	41
6.1 Introduction	41
6.2 Flow setup	42
6.2.1 Boundary Condition	43
6.2.2 Grid Resolution	44
6.3 Results	44
6.3.1 Signed-Distance Field	44
6.3.2 Grid Convergence	45
6.3.3 IBM Forces	47

6.3.4	Mean Velocity	48
6.3.5	Corrected Reynolds Stress	49
7	Conclusion and Future Work	55

Introduction

Since 2018, more than half of the world's population resides in urban areas, with the most urbanized geographic regions located in Northern America, Latin America and the Caribbean, and Europe. According to (UNDESA, (2018)), by 2050, a population growth of around 2.5 billion is predicted, along with a 13% increase of the percentage of the global urban dweller. This brings challenges to urban development efforts by governments, urban planners, and stake holders in order to improve the quality of life and promote sustainable growth of urban areas (Cf, 2015).

Urbanization is accompanied by the spatial expansion of the urban settlement through the transformation and the annexation of the rural regions (UNDESA, (2018)). The replacement of the rural and natural surroundings by their urban counterparts results in a significant change of the geometry and the content of the area. This leads to changes in the transport of air, moisture, pollutant, and heat etc, thereby altering the characteristics of the local atmospheric boundary layer, which locates at the lowest part of the atmosphere and is in direct contact with ground surface. As a result, urban structures create their own unique microclimates, such as Urban Heat Island (UHI) effect (Manley, (1958)). Urban flow is a crucial factor to evaluate in terms of the planning of new urban areas as it influences the local microclimate through a series of phenomena such as wind-driven rain, pollutant dispersion, building ventilation, and pedestrian wind condition around buildings (Gunawardena et al., (2017)). It has become a requirement for the design of high-rise buildings to pass the wind comfort and/or safety criteria for the building designers and urban planners (Blocken et al., (2012)).

Various measurement methods can be used to assess the wind condition for urban areas, this generally includes field measurements and wind tunnel measurements. The former approach is typically conducted by placing probes at certain locations to collect data such as temperature, humidity, and solar radiation (Krüger et al., (2011)), as well as placing anemometers to obtain wind speed and direction (Dye, (1980); Kamei and Maruta, (1979)). The advantage of field measurement is that it generates robust data that accurately represents the actual flow field. However, field measurement is only limited to certain wind station measurement locations in existing urban areas, resulting in the inability of capturing the entire urban flow field and predicting flow in the newly designed urban districts. In addition, full-scale measurement sometimes is insufficient for validation data because of its practical challenges of being subject to altering meteorological phenomena (Mittal et al., (2018)), while typically benchmark data under well-controlled conditions are preferred.

The wind-tunnel approach generally involves wind tunnels testing with scaled-downed models. Various flow measurement techniques has been applied to conduct researches with high resolution, including Hot-Wire Anemometry (HWA) (Uematsu et al., (1992)), Hot-Film Anemometry (HFA) (Stathopoulos and Storms, (1986)), Irwin probes (Zhang et al., (2017) and Zhang et al., (2017)), infrared thermography (M. Yamada et al., (1996)), Laser Doppler Anemometry (LDA) (Lam, (1992)), and Partical Image Velocimetry (PIV) (Allegrini and Lopez, (2016)). Wind tunnel approach is advantageous in understanding a wide range of complex phenomena by obtaining detailed data through controlling geometric structures and flow variables at wishes (Ahmad et al., (2005)). Nonetheless, wind tunnel measurements may still be

only able to provide data at a small set of points, and thus may not be effective at providing the full history of the flow. In addition, it suffers from incompatible similarity problems when compared with full-scale measurements, as reported by (Blocken et al., (2012)). Finally, physical models are limited to the overall geometry of the studied area, with challenges of including detailed urban components such as street dimensions, vegetation composition, landscape, surface roughness, which can alter from time to time in real urban areas (Ahmad et al., (2005)).

Another popular approach that goes hand-to-hand with experimental campaigns is to use Computational Fluid Dynamics (CFD) to predict the urban flow dynamics. The advantage of using CFD lies in its ability to give the detailed 3D wind field directly around the geometry of interest (Blocken and Carmeliet, (2004)). Although validation is required, various complex factors can be accounted for in CFD models. This includes the detailed shape and orientation of urban structures, vegetation, as well as heat generation (Vanky et al., (2023)). In addition, it is less time-consuming and less expensive compared with wind tunnel approach (Mittal et al., (2018)).

To summarize, understanding the flow condition within urban areas is important for urban planners to design living places that are safe and comfortable for their residences, as well as creating sustainability and clean environment. To facilitate this process, CFD, as an emerging attractive method, can contribute significantly to the detailed analysis of turbulent flow around buildings and to study the influence of various factors.

2

Literature review

2.1. Urban Microclimate

With the rapid global urbanization, studies on the dynamics of urban microclimate are gaining popularity. Urban microclimate is influenced by factors both external and internal of the city. The external macroclimate may have a significant impact on the local urban climate in terms of wind, temperature, humidity, and precipitation (Jian et al., (2022)). For example, under the influence of temperate maritime climate, the Netherlands, with its near-sea location and flat terrain, has rainy and windy winter and makes it hard to bicycle.

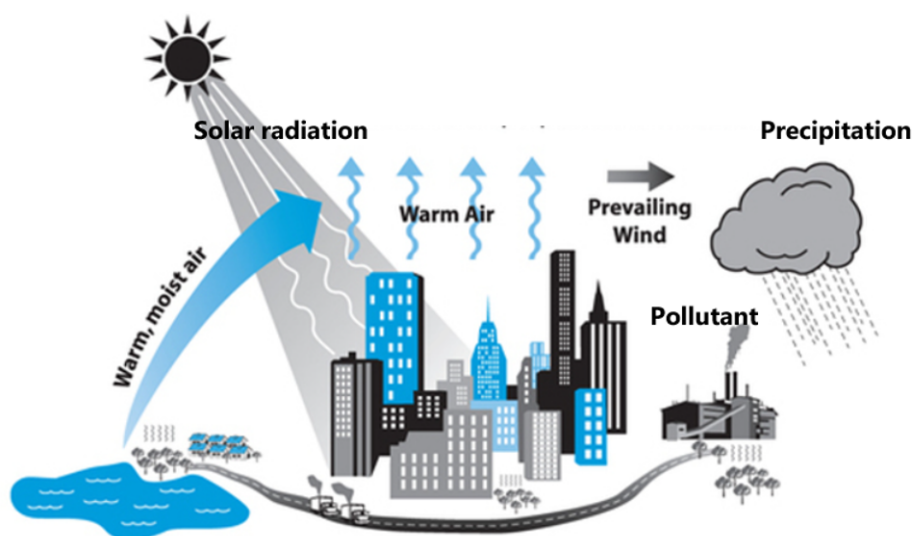


Figure 2.1: Schematic of urban microclimate. (Taken from <http://geographylaunchpad.weebly.com/>)

Understanding the complicated interactions between different factors within urban areas is also crucial for studying urban microclimate. This generally consists of the layout and the geometry of landscapes, the presence of vegetation, water bodies, and other urban furniture (Dimoudi et al., (2013)). These features strongly influence all the different urban-area transport dynamics in terms of mass and heat transfer, such as air flow, pollutant dispersion, heat convection and radiation, cloud formation and movement, which in result could raise urbanized-area issues, such as wind-driven rain, pollutant dispersion, building ventilation, and hazardous ground-level wind (Gunawardena et al., (2017)). A schematic of urban microclimate is shown in Figure 2.1. An example regarding the impact of landscapes can be demonstrated with orographic precipitation. When moist air approaches a barrier, the moist air rises over it, cools, and reaches its saturation point, leading to the condensation of water vapor into clouds. Consequently, this results in the subsequent release of precipitation in the form of rain or snow (Cengiz,

(2013)).

2.2. Pedestrian-level Wind

Urban microclimate can be studied at various spatial scales, ranging from the global scale to indoor environment and human thermophysiology. The computational domain of global scale is typically larger than 2000 km till the dimension of the entire globe (6500 km) (Yamada and Koike, (2011)). Mesoscale ranges from 2 km up to a few hundred kilometers (Blocken, (2015)) by having typically a domain size of 50 km to 2000 km and grid resolution of 1 km to 100 km (Yamada and Koike, (2011)). Enriched with detailed meteorological phenomenon such as cloud formation and radiation, the numerical models to explore atmospheric events, for instance, thunderstorms and precipitation bands, are often referred to as Mesoscale Meteorological Models (MMM). (Pielke Sr, (2013)). However, in MMM, several contributing building details, such as building geometry and street canyons, are generally oversimplified and not modeled explicitly (Toparlar et al., (2015)).





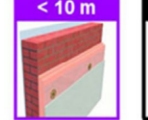
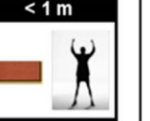
Spatial scale	Global	Mesoscale	Microscale	Building	Component	Material/Human
Distance	< 6500 km 	< 200 km 	< 2 km 	< 100 m 	< 10 m 	< 1 m 
Model cat.	NWP	NWP / MMM	CFD	CFD / BES	BC-HAM	MSM / HTM

Figure 2.2: Schematic representation of the spatial scales relevant to building simulation, including their typical maximum horizontal length scales and associated model categories. NWP = Numerical Weather Prediction; MMM = Mesoscale Meteorological Model; CFD = Computational Fluid Dynamics; BES = Building Energy Simulation; BC-HAM = Building Component – Heat, Air, Moisture transfer; MSM = Material Science Model; HTM = Human Thermophysiology Model (The figure is taken from Blocken, (2018)).

The smaller scales are called microscales and have horizontal domains that are often smaller than 2 km with the spatial resolution between 0.1 m and 100 m (Blocken, (2015)). This is the range where the modeling of urban physics generally takes place. By taking into account of various complex urban structures, such as plants, benches, bushes, and sidewalks, CFD methods are able to predict the detailed wind flows and assess pedestrian wind comfort as well as pollutant dispersion (Blocken, (2015)).

Building scale (< 100 m) focuses on the impact of building components on the outdoor and indoor environment interaction (Zheng et al., (2020)). Component scales (< 10 m) and human scales (< 1 m) generally aim to investigate indoor climate and its impact on human being (Fiala et al., (1998)).

2.3. Wind Comfort Criteria

For decades, high-rise buildings have been in favoured by urban planners in order to accommodate more people in densely populated urban areas. However, high-rise buildings tend to transport the air flow from the high altitude down to the ground level through standing vortices, forming high wind speed regions at building corners. This produces uncomfortable and sometimes even dangerous wind conditions for pedestrians (Penwarden and Wise, (1975)). Hence, it is important for city planners to consider wind comfort condition in the design of livable accommodations.

Many factors contribute to the perceptive comfort of pedestrian, such as temperature and humidity, while the mechanical effect of wind is the one that is considered the most important (see W. Melbourne, (1978) and Willemsen and Wisse, (2007)). Wind comfort criteria provides guidelines and standards to assess the level of comfort or discomfort that people experience when exposed to wind in outdoor spaces. It typically consists of wind speed and a maximum allowed exceedance probability, which assesses wind speed fluctuation (W. H. Melbourne, (1971)), followed by a set of outdoor activities, such as sitting and walking.

Various wind comfort criteria exist (see Janssen et al., (2013) ,W. H. Melbourne, (1971), and Hunt et al., (1976)). Large differences may be found between different criteria since most of them have

Category	Mean velocity	Probability	Activity
A	5 m/s	< 2.5%	Sitting Long
B	5 m/s	< 5%	Sitting Short
C	5 m/s	< 10%	Walking Leisurely
D	5 m/s	< 20%	Walking Fast
E	5 m/s	\geq 20%	Uncomfortable

Table 2.1: NEN8100 wind comfort for a neutral atmospheric boundary layer and isothermal condition (Comfort, (2006)).

been based on people's intuition (Blocken and Carmeliet, (2004)). Dutch wind nuisance standard NEN 8100 (Comfort, (2006)) is preferred because it is the latest one for assessing pedestrian wind comfort. Shown in Table 2.1, it presents exceedance probabilities and corresponding activities based on a 5 m/s wind speed. This speed is identical for level 3 and level 4 according to Beaufort Wind Scale (According to Water, (2005), under wind speed 5 m/s people start to perceive wind as uncomfortable. At level 3, "dust gets blown up", and at level 4, "hair messed up, clothes flapping").

2.4. CFD Methods

Urban flows can be studied mainly by three CFD methods, Reynolds-Averaged Navier Stokes (RANS), Large Eddy Simulation (LES), and Direct Numerical Simulation (DNS). Choices have to be carefully made between different turbulence models, subgrid-scale models, land surface fluxes, boundary and initial conditions, as well as discretization schemes.

2.4.1. RANS

Reynolds-Averaged Navier Stokes (RANS) is the most widely used model for the numerical study of urban microclimate (Toparlar et al., (2017)). In RANS, all scales of turbulence motion are modeled. The flow variables are decomposed into mean and fluctuating components. In RANS, only the mean flow is explicitly solved, and the fluctuating components are treated as separate terms called Reynolds stress tensor, representing the turbulent effect on the mean values. Closure hypotheses are introduced to relate the Reynolds stress tensor with the mean flow characteristics to iteratively solve the RANS equations. Various commonly used models for different methods are listed in Table 2.2.

CFD Method	Commonly used models
DNS	
LES	Standard Smagorinsky-Lilly model (SSL) Dynamic Smagorinsky-Lilly model (DSL) Wall-Adapting Local Eddy-viscosity model (WALE) Dynamic Kinetic Energy model (DKE)
RANS	Standard $k - \epsilon$ model Yamada and Mellor $E - \epsilon$ model RNG $k - \epsilon$ model Realizable $k - \epsilon$ model $k - \omega$ Shear Stress Transport ($k - \omega$ SST)

Table 2.2: Commonly used CFD models for the study of urban microclimate. (see Toparlar et al., (2017) and Jianlin et al., (2019))

In RANS, the most used models are the Standard $k - \epsilon$ model and the Yamada and Mellor $E - \epsilon$ model, where E represents the energy density of the wave field. The former introduces a two-equation model that involves Turbulent kinetic Energy (TKE) k and turbulent dissipation rate ϵ . It has gained wide popularity due to its robustness, computational efficiency and acceptable accuracy for industrial flow problems (Jones and Launder, (1972)). However, it is based on empirical conclusions that rely on phenomenological observations. Nonetheless, the latter is most often used for ocean modeling. In terms of urban flows, standard $k - \epsilon$ model suffers from the overestimation of TKE in the building windward face. It also underestimates the wake regions, as well as flow separation and recirculation around buildings.

Various revised $k - \epsilon$ models are also investigated regarding urban flows, such as RNG $k - \epsilon$ model (Yakhot and Orszag, (1986)) and Realizable $k - \epsilon$ model (Shih et al., (1995)). They both show improvement in high-speed regions, however, have more or less accuracy issues at wake regions (Blocken and Carmeliet, (2008)). Yamada and Mellor $E - \epsilon$ model is another widely used model (Yamada and Mellor, (1975)). However, although not recommended (Toparlar et al., (2017)), it has gained popularity because it is the only available turbulent model in ENVI-Net, a microclimate simulation software (Bruse and Fler, (1998)). $k - \omega$ Shear Stress Transport ($k - \omega$ SST) also exhibits good performance, but it overpredicts the flow separation and underestimates the TKE (Rajasekarababu et al., (2022)).

It can be concluded that the main limitation of RANS is that it filters out many details of transient turbulent motions that are essential to the analysis urban microclimate. Nonetheless, the current computing capability allows researchers to do much better.

2.4.2. LES

In Large eddy simulation (LES), the large-scale turbulent structures are resolved on the computational grids, while the smaller scales are modeled using subgrid-scale (SGS) model. The SGS model describes the flux of momentum, mass, or heat associated with scales which have been filtered. LES is well-suited for simulating turbulent flows in which the large-scale eddies are of primary focus, for example, atmospheric boundary layer and wake behind bluff bodies (Stoll et al., (2020)). LES is becoming increasingly popular in studying urban microclimate due to its ability to capture the unsteady, time-dependent turbulent behaviors, at the same time being more accurate than RANS and less computationally expensive than DNS. This make LES a powerful tool for understanding the physics of turbulent structures in urban flows. A popular SGS model is Vreman eddy viscosity model (Vreman, (2004)), this will be described in Chapter 3.

2.4.3. DNS

Direct numerical simulation (DNS) resolves all ranges of the turbulent fluctuating motion and provides in every detail the simulated results for non-linear mechanisms of turbulence production and dissipation. Hence, no turbulent closure schemes are needed. However, smaller turbulent motions can only be resolved by smaller cell size. The cell number increases significantly with the increase of Reynolds number. Besides, time step should decrease too, so that the number of iteration over time increases, making DNS extremely computationally expensive especially for the geometry that has high Reynolds number (Barulli, (2022)). Previous studies using DNS would be discussed in the following sections. In microscale urban flow simulation, the required domain is usually too large for DNS to be feasible for interpreting all the complex turbulence structures (Palme and Salvati, (2021)).

2.4.4. Immersed Boundary Method

While having the advantages stated above, LES has long computing time. The main reason for the increased computational expense in LES compared with RANS is the need for smaller grid size. Since LES aims to capture the energy-containing turbulent eddies, the grid resolution should be fine enough to capture the size and dynamics of these eddies accurately. This requires a higher number of grid points compared to RANS simulations, in which the turbulence is modeled based on averaged quantities.

Immersed Boundary Method (IBM) was originally developed (Peskin, (1982)) to model the flow around deformed structures. One of the key features of IBM is that a continuous grid is used. The computational grid is not necessarily to be conformed with the physical boundary in general, thus eliminating the time-consuming meshing procedure for modeling complex geometries. Mathematical method, for example Signed-Distance Field (SDF) method, can be applied to couple the structure boundary and the mesh.

$$\frac{\partial u_i}{\partial x_i} = 0, \quad (2.1)$$

$$\rho \left(\frac{\partial u_i}{\partial t} + \frac{\partial u_i u_j}{\partial x_j} \right) = -\frac{\partial P}{\partial x_i} + \mu \frac{\partial^2 u_i}{\partial x_j^2} + f_i \quad (2.2)$$

In IBM, the presence of the immersed boundary needs to be introduced into the governing equations. Locally forces are added near the boundary to approximately enforce the no-slip or no-penetration condition on the boundary. This process is easily done by adding a source term in the momentum equation, denoted as \mathbf{F} in equation 2.2. \mathbf{F} is defined as the integral of body force density multiplied by the kernel of local interaction, which represents the force that is applied by the immersed boundary to the fluid flow.

2.5. Focus of the Present Studies

The turbulent motions are of most interest regarding the studies on pedestrian wind comfort and pollutant dispersion. Hence, the focus of the present research is restricted to neutral atmospheric boundary layer conditions by studying the influence of urban structures on the dynamics of air flow, while the thermal and moisture convection behaviors are neglected.

The topology of urban areas alters the speed and direction of the wind. As a result, urban wind patterns differ from those in rural areas, farmlands, and forests. It is commonly believed that high-rise buildings obstruct the flow of air, leading to reduced wind speed in streets, increased air pressure, and worsened ventilation, among other negative effects on the city. However, tall buildings could sometimes increase the wind speed.

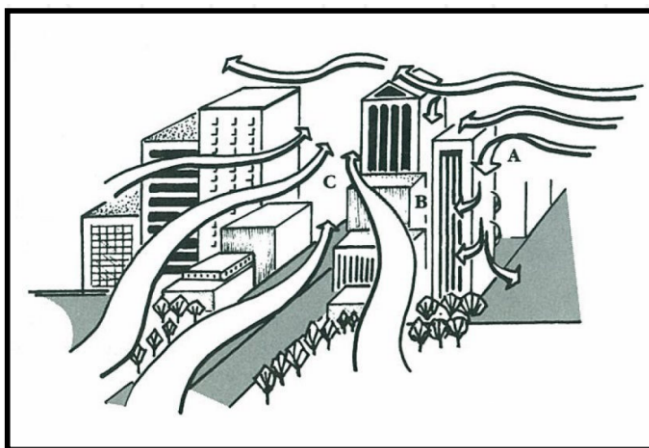


Figure 2.3: Urban air flow (Cengiz, (2013)).

Three common forms of urban air flow are shown in Figure 2.3 (adapted from Cengiz, (2013)). A: When the wind goes perpendicularly towards the front of a standalone high-rise building, the higher-level air flow is transported down to the ground, resulting in increased wind speed at the ground-level due to the conservation of mass. This phenomenon will be described in more detail in the next paragraph. B: When the spacing between two high-rise buildings is small, the kinematic energy of the wind is maintained at higher-level. Air flow from the upstream cannot enter the small air pocket of the street, causing a calm air zone between the two buildings. C: This shows air flow passing through the channels of a street canyon. The flow velocity increases within the channel due to mass conservation. However, complex turbulence forms behind the buildings. Significant physical mixing and exchange phenomena can be observed in terms of both momentum and mass of air and pollution (Zhou and Hanna, (2007)). The turbulence phenomenon brings challenges to the prediction of urban flows and the consequential issues such as pedestrian wind comfort.

2.5.1. Flow Around a Single Building

A typical flow pattern around a single high-rise building is studied with wind tunnel measurements (Beranek and Van Koten, (1979)). The schematic is adapted from another research (Blocken and Carmeliet, (2004)). When the wind approaches the high-rise building perpendicular to its surface, part of the flow circumvents the building from above (1) and around its sides (2, 9). A stagnation point forms at the upper part of the windward face (Klotz, (1986)). Air diverges toward different directions (3, 4), and (5). The downward moving flow creates a series of pedestrian-level standing vortex (6), which reduces

the wind speed at location (7). The standing vortex stretches laterally and creates high-speed areas at corners (8). A wake region with low pressure and recirculation (10,13) is observed at the back side of the building. The wake region ends at another stagnation point, which marks the far downstream region (12). The pronounced velocity gradients lead to the formation of small vortices (16). Areas of high wind speed often raise concerns related to pedestrian comfort, while the low-pressure zone on the leeward side can lead to issues such as pollutant concentration.

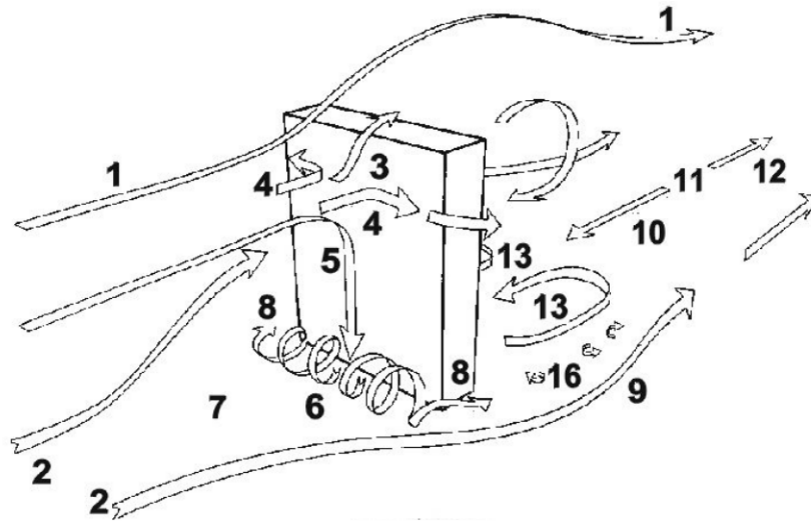


Figure 2.4: Wind flow around a single wide high-rise rectangular building.

Studies has also shown that the geometry of building surface has a significant impact on the flow around it. For example, clockwise recirculation was observed above the stagnation point, while anticlockwise recirculation was observed below the stagnation point on the windward facade on the building with balconies (Zheng et al., (2020)). Additionally, the “zigzag” facade appurtenances were studied experimentally. It was demonstrated that these appurtenances can effectively control vortex shedding. Specifically, the vortex peak of the power spectra of “zigzag” appurtenances is higher, and its bandwidth is narrower. Furthermore, horizontal plates were found to have a greater impact on managing vortex shedding than vertical plates, since the vertical convection and diffusion are restricted, and the vortex intensity is thus reduced (Hui et al., (2019)).

2.5.2. Street Canyons

The nonlinear mechanism of the urban air flow in street canyons is one of the interesting study areas. DNS were scarcely used on the street canyon mainly due to its high computational cost. However, it can be achieved by using the models which are scaled-down to moderate Reynolds numbers, through either decreasing the dimension of the geometry or lowering the wind speed given constant air viscosity. In the notable work done by Coceal et al., (2006) (see also Coceal, Dobre, and Thomas, (2007), Coceal, Thomas, and Belcher, (2007), Coceal et al., (2014), and Castro et al., (2017)), flow over cubic, urban-like, and fully rough regular arrays having Reynolds number $Re = 5000$ was studied based on the free stream velocity and the cubic height. A schematic of the flow geometry is shown in Figure 2.5. By employing a formal spatial averaging procedure, they were able to interpret the flow within the street canyons, as well as the flow above it as a rough wall boundary layer. The mean velocities, stresses and other parameters showed excellent agreement with the wind tunnel experiments, in which the cubic layout greatly influences the turbulent structures. The study also emphasized the significant impact of unsteady turbulent effect within the lower canopy layer, drawing attention to unsteady effect from the steady mean flows. Additionally, it was concluded that the surface roughness can be seen as porous obstacles such that the flow is formed by the interaction with the wakes. This exerts an aerodynamic drag on the main flow. However, a problem associated with DNS is that the Reynolds numbers are much smaller than the cases for real urban areas. Considering the high computational costs of DNS, it is still limited to moderate Reynolds numbers and still impossible to apply in real urban areas (Cotella

Dalmau et al., (2016)).

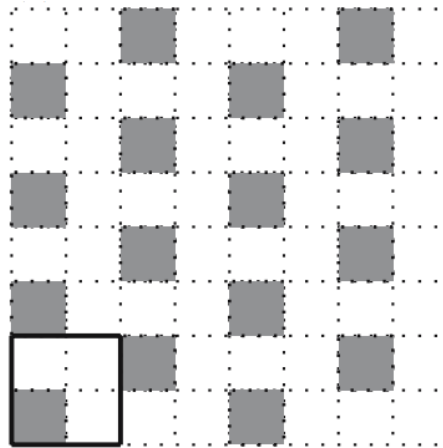


Figure 2.5: An example: cubic, urban-like street canyon arrays with staggered arrangement ($8h \times 8h \times 4h$, with h the cube height), the box with bold lines indicated repeating units (Coccal et al., (2006))

The responses of the neutrally stratified boundary layers to a roughness transition in an array of cubes with in-line arrangement was studied numerically (see Tomas et al., (2016)) with fully-developed flow periodic boundary condition in the streamwise direction. The study utilized a modified LES code known as Dutch Atmospheric Large-Eddy-Simulation (DALES, Heus et al., (2010)). Enriched with an Immersed Boundary Method (IBM) (Pourquie et al., (2009)), the code incorporates the Boussinesq approximation in the original Vreman model (Vreman, (2004)). The inflow condition was generated using a modification of the recycling method that was studied by Lund et al., (1998) and Kong et al., (2000). Validated with the measurement data (Castro et al., (2006)), the study found that under neutrally buoyant and stable conditions, the surface forces converged to similar values after seven streets downstream from the start of the array. In the neutral condition case, the mean streamwise velocities were essentially the same as those obtained with the fully-developed boundary condition. However, according to the results for the Turbulent Kinetic Energy (TKE), it took a much longer distance for the stable boundary layer. The author attributed this to the stratification effect, which resulted in less buoyancy destruction of TKE within the internal boundary layer. In addition, the stable condition causes more pollutant concentration in the arrays due to the decrease of streamwise advection, as well as the slower growth of the internal boundary layer so that the advection of pollutants is limited.

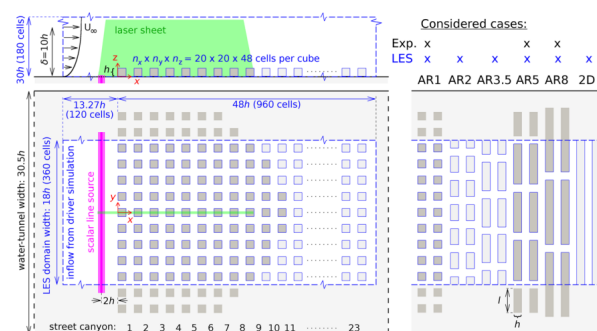


Figure 2.6: A schematic of the experimental and numerical model by Tomas et al., (2017).

Another study (see Tomas et al., (2017)) focuses on the flow and pollutant diffusion in the rural-to-urban morphology with a stable inlet boundary condition. Different spanwise length scales of the roughness are also modeled. The Vreman model (see Vreman, (2004)) uses the same with the previous study by Tomas et al., (2016). One of the advantages of using Vreman model over Smagorinsky–Lilly model is that it does not need wall damping. The filtered mass conservation, momentum and concentration transport equations for incompressible air flow can be written as follows:

$$\begin{aligned}
\frac{\partial \tilde{u}_i}{\partial x_i} &= 0, \\
\frac{\partial \tilde{u}_i}{\partial t} &= -\frac{\partial \tilde{u}_i \tilde{u}_j}{\partial x_j} - \frac{\partial}{\partial x_i} \left(\frac{\tilde{p} + \tau_{kk}/3}{\rho} \right) + \nu \frac{\partial^2 \tilde{u}_i}{\partial x_j^2} + \frac{\partial}{\partial x_j} (2\nu_{sgs} S_{ij}), \\
\frac{\partial \tilde{c}^*}{\partial t} &= -\frac{\partial \tilde{c}^* \tilde{u}_j}{\partial x_j} + \frac{\nu}{Sc} \frac{\partial^2 \tilde{c}^*}{\partial x_j^2} + \frac{\partial}{\partial x_j} \left(\frac{\nu_{sgs}}{Sc_{sgs}} \frac{\partial \tilde{c}^*}{\partial x_j} \right) + S,
\end{aligned} \tag{2.3}$$

where the overline sign represents filtering operation, c is the pollutant concentration, τ_{kk} is the trace of the SGS stress tensor, ν_{sgs} is the SGS eddy viscosity, S_{ij} is the rate of strain, Sc_{sgs} is the SGS Schmidt number, and S is the source term. The CFD work is carried out alongside with water tunnel experiments. It is found that the spanwise extent of the obstacles does not significantly affect the distance that it takes for the flow to adapt to the surface roughness. However, the large scale secondary flows associated with the spacing of the array could cause the delayed convergence of the surface forces over roughness. Additionally, the pollutant flux in the canopy layer can be significantly influenced by the advective pollutant flux in the first three rows, which suggests the impact of the roughness transition on the pollutant dispersion. This is similar to the fully developed boundary condition case.

The building geometry and the street canyon layout are crucial factors. Using LES, Kluková et al., (2021) investigated for the first time the crucial combining effect of the roof shape, roof-height non-uniformity, and source position on the pollutant transport between 3D urban array. Six different arrangements of building heights were examined. The "Extended Large-Eddy Micro-scale Model" (ELMM) developed by Nosek et al., (2018) was used to handle the transient scale transport around complex obstacles by solving Navier-Stokes equations. They found that the street canyon with flat roofs produces more vertical recirculation, which hinders the upstream air from flowing into the canyon, which leads to more pollutant accumulation. However, the ventilation within street canyon with pitched roofs is mainly caused by turbulence motions. This results in better transfer of pollutants out of the canyon. In a separate investigation, Chew and Norford, (2018) studied the effect of void decks on enhancing pedestrian-level wind speed in urban street canyons with both RANS ($k-\epsilon$) simulation and water tunnel measurement. The concept behind this study is that the shops on the ground floor can be replaced by the void deck. The findings indicates that the use of void decks can lead to a doubling of pedestrian-level wind speeds. Furthermore, the height of the void decks plays a significant role in affecting the flow speeding inside of the street canyons before transition. However, the alteration of aspect ratio does not induce a noticeable change in flow speeds.

Another study highlighted that the lack of accurate traffic-induced turbulence parameterizations can lead to the overestimation of pollutant concentrations at the street level (Di Sabatino et al., (2003)). Through including the mass transfer equation, pollutant dispersion in traffic flow is studied with RANS and LES using a quasi-steady method. Based on an assumption that an additional momentum source comes from drag force exerted by the air to the moving vehicles, this method is suitable for modeling moving traffics. Standard $k-\epsilon$ model is found to be suitable for this type of study considering the computational cost, while LES with the Wall-Adapting Local Eddy-viscosity (WALE) model outperforms all others models (Katolický and Jicha, (2005)).

It was seldomly evaluated which method is suitable for what kind of urban flow. In a study (see Jianlin et al., (2019)), various LES models were examined on a 3 cubic arrays. The study considered four SGS models that are available in ANSYS, standard Smagorinsky-Lilly model (SSL), the dynamic Smagorinsky-Lilly model (DSL), the wall-adapting local eddy-viscosity model (WALE), and the dynamic kinetic energy model (DKE). Each case has its specifically adjusted mesh according to the Best Practice Guideline (BPG (Tominaga et al., (2008))). The results indicated that all SGS models slightly underrated the pedestrian-level-wind mean velocities in the wake region. The DSL model exhibited the closest agreement with the wind tunnel measurement data in terms of mean velocities. On the other hand, the DKE model tended to underestimate the mean velocities. WALE and DKE models overestimated the turbulent fluctuations in the wake region.

Boundary conditions can be adjusted by taking the mean of a period of meteorological data from wind station measurements (Vanky et al., (2023)). Wind comfort criteria were included in this numerical

study using RANS model with IBM. It was validated with wind tunnel measurement. Furthermore, A Reynolds number independence test was performed with $Re = 17,000$ and $Re = 170,000$, with the latter typically a more realistic urban environment. The results show that the Reynolds number independence is achieved.

The existence of surrounding buildings also has a significant impact on the urban area due to the sheltering and channeling effects they create. To take this into account, most studies treated the target area with detailed building configurations and the surrounding regions with surface roughness.

The effect of surrounding buildings was investigated using a real urban area in Dalian, China, by comparing a full-scale model with its simplified counterparts (S. Liu et al., (2018)). The simplification was made by grouping the nearby regions into five different roughness lengths based on building density and building height. Meteorological data was adopted for boundary conditions. A 5.5% discrepancy was found in the mean velocity between the simplified model and the full-scale model, suggesting that the approximation using only roughness is not fully accurate to represent the surroundings. The author also suggested that the CFD domain should be three times larger than the target building length scale. However, the simulation was carried out using RANS. Future research efforts should focus on refining the modeling approaches and incorporating more advanced turbulence models to enhance the accuracy of predictions.

2.5.3. Actual Urban Areas

Simulation of real urban areas generally combines statistical meteorological data, aerodynamic knowledge, and the subsequent wind comfort assessment. A decision flowchart was developed to specify the decision steps that are essential to analyse wind comfort using CFD methods ((Blocken et al., (2012))). Three cases were specified depending on whether the site has been constructed and the availability of the field-measurement data. The flow chart serves as an excellent supplement to the existing BPG. The designed workflow is followed by a case study of wind comfort conditions at Eindhoven University campus using Steady RANS realizable $k - \epsilon$ model. Another practice of this is demonstrated with a simplified model of Bergpolder Zuid, Rotterdam, a place that was planned to be renovated to promote its resilience to heat waves in summers (Toparlar et al., (2015)). 3D URANS with realizable $k - \epsilon$ model was applied. The simulated surface temperatures have only an average of 7.9% difference from that measured using thermal infrared satellite images. However, the simplified model does not take into account the existence of plants and urban furniture. Another issue is related to the inlet boundary conditions. It is usually difficult to obtain the boundary conditions in an actual urban area. While reasonable velocity and temperature profiles are assumed, they may not perfectly match the actual conditions, which are often characterized by unstable stratification and spatial inhomogeneity. Another case study at IJmuiden sea lock proves that the method can be also used in sea shore regions. The ocean is characterized by its long roughness length, and the transition of the roughness length from the sea to the dense docks is drastic (Ricci and Blocken, (2020)). According to the study, large discrepancy between CFD and field measurement was obtained. The complex wind condition in this area makes it insufficient to use RANS realizable $k - \epsilon$ model to capture the detailed flow structures.

2.6. Research Outline

This thesis aims to explore a novel approach to modeling flows over complex urban areas. The development of the research is based on three stages. A schematic of the logic flow is demonstrated in Figure 2.7.

In the first stage, an eddy viscosity model is implemented in CaNS. The eddy viscosity is incorporated into the NS equation as an extra diffusion term after precise interpolation due to the staggered grid arrangement. The added diffusion term is discretized with a second-order finite difference scheme. The model is validated with turbulent channel flow. Channel flow data is available in online database as well as in the paper by Vreman, (2004).



Figure 2.7: A logic flow chart that the study follows. In the green boxes are the status for the development of the code and the geometry that is being used for the verification or computation. The red text are the major developments that were made in each step. The validation steps are marked with blue "V".

The project aims to tackle complex geometries by using IBM, and to investigate SDF as a convenient tool to connect the structural boundary representation with IBM implementation. In the second stage, such approach is substantiated through validation with flows over periodic cube arrays. The IBM adopts a direct forcing approach by approximating the effect of the structure boundary as an added force term in NS equation. SDFs are computed with a novel program "STL2SDF". The approach is solidly validated in this step.

Subsequently, such method can be applied for models that represent actual urban feature. In the campus of Delft University of Technology (TU Delft). Strong or even dangerous wind is often complained at the crossroad near the so-called EWI building. The building is 98– meter high at the center of the TU Delft campus, indicated with a red box in Figure 2.8.



Figure 2.8: A bird view of TU Delft campus, the red box denotes the EWI building. and the yellow star represents a the crossroad where people experience strong wind during winter (the picture is taken from <https://www.facebook.com/TUDelftCampusLife/photos/a.265076050701266/540351696507032/?type=3>).

In the third step, such problem is explored as an application of the validated approach on actual urban areas. A simplified 3D model of TU Delft campus is scaled down to an achievable Reynolds number. Considering a potential future wind tunnel test, the dimension of the model is adjusted according to an existing wind tunnel boundary layer test section. This step is going to explore the wall-resolved LES by a grid-convergence study, in which turbulence characteristic are analyzed.

3

Numerical Methods

3.1. Introduction

The Navier-Stokes (NS) equations naturally describe the chaotic and multi-scale dynamics of turbulence. The smallest turbulence structures range down to the Kolmogorov length scale $\eta = (\frac{\nu^3}{\epsilon})^{1/4}$ that has to be resolved by a grid resolution of the order of η (see Moin and Mahesh, (1998)). Resolving such scale requires Direct Numerical Simulations (DNS) which provides deeper insights to the turbulence phenomena, however, puts high demands for the computer power.

With the development of computer power as well as more efficient numerical methods, computations of complex turbulent flows in larger domains become possible. In the present study, Canonical Navier-Stokes (CaNS) is used. CaNS, developed by Costa, (2018), is a numerical tool for massively parallel DNS of incompressible Newtonian fluid flows on up to $O(10^5)$ CPUs and $O(10^4)$ GPUs. The code uses a very efficient FFT-based solver for the second-order finite-difference Poisson equation in a 3D Cartesian grid. It covers Neumann, Dirichlet, and Periodic boundary conditions, and offers flexibility in tuning the grid resolution. The excellent performance of CaNS has been demonstrated on some major GPU-accelerated clusters such as Perlmutter, Summit, and Marconi 100. Up to 10^4 cores can run in parallel for a domain with 10^9 spatial degrees of freedom, with very small wall-clock time/time step.

3.2. Governing equations

CaNS concerns the incompressible Navier-Stokes (NS) equation:

$$\frac{\partial u_i}{\partial x_i} = 0, \quad (3.1)$$

$$\frac{\partial u_i}{\partial t} + \frac{\partial u_i u_j}{\partial x_j} = -\frac{1}{\rho} \frac{\partial P}{\partial x_i} + \nu \frac{\partial^2 u_i}{\partial x_j^2}, \quad (3.2)$$

where u is the velocity, P is the total pressure, and ν is the kinematic viscosity. Density ρ is assumed unity.

Pressure-correction (or Fractional-step) method is used to couple the pressure and velocity (see Kim and Moin, (1985)). This is incorporated into a third-order low-storage Runge-Kutta (RK3) for time advancement (see Wesseling, (2009)). The diffusion terms are treated explicitly for low Reynolds numbers to increase since only high Reynolds numbers are concerned in this study. The RK3 method can be written as:

$$\frac{u_i^* - u_i^k}{\Delta t} = \left(\alpha_k \mathbf{AD}^k + \beta_k \mathbf{AD}^{k-1} + \gamma_k \frac{\partial p^{k-1/2}}{\partial x_i} \right), \quad (3.3)$$

$$\frac{\partial^2 \Phi^k}{\partial x_i \partial x_i} = \frac{1}{\gamma_k \Delta t} \frac{\partial u_i^*}{\partial x_i}, \quad (3.4)$$

$$u_i^k = u_i^* - \gamma_k \Delta t \frac{\partial \Phi^k}{\partial x_i}, \quad (3.5)$$

$$p^{k+1/2} = p^{k-1/2} + \Phi^k, \quad (3.6)$$

where the term AD contains convective and viscous terms. u^* is the prediction velocity and Φ is the correction pressure. k is the substep time advancement index that ranges from 1 to 3. α_k , β_k , and γ_k are RK3 coefficients with values $\alpha_1 = 8/15, \alpha_2 = 5/12, \alpha_3 = 3/4; \beta_1 = 0, \beta_2 = -17/60, \beta_3 = -5/12; \gamma_1 = 8/15, \gamma_2 = 2/15, \gamma_3 = 1/3$. The last equation $p^{k+1/2} = p^{k-1/2} + \Phi$ suggests the staggered arrangement in time.

The time step limit is enforced to ensure stable temporal integration. The maximum time step is set according to Wesseling, (2009):

$$\Delta t_{max} = \min \left(\frac{1.65 \Delta r^2}{\nu}, \frac{\sqrt{3} \Delta r}{\max_{ijk} (|u| + |v| + |w|)} \right), \quad (3.7)$$

where $\Delta r = \min(\Delta x, \Delta y, \Delta z)$ means the minimum of the grid spacing in three directions. In CaNS solver, the maximum CFL number and the minimum timestep can be customized by users to suit different needs. The time step applies to explicit time advancement of the diffusion terms for the current study, as the Reynolds numbers are high.

3.3. Subgrid Scale Model

The numerical methods used for DNS CaNS can be also utilized by a Large Eddy Simulation (LES) with CaNS. The current study applies Vreman model as the subgrid scale (SGS) eddy viscosity model. Vreman model uses grid itself as the filter (see Vreman, (2004)), which makes it convenient to implement in CaNS. The scales of the eddies larger than the grid resolution are explicitly resolved, and the smaller ones are modeled. In this model, an extra eddy viscosity term is added in the filtered NS equation. The filtered equation can be written as follows:

$$\frac{\partial \tilde{u}_i}{\partial x_i} = 0, \quad (3.8)$$

$$\frac{\partial \tilde{u}_i}{\partial t} + \frac{\partial \tilde{u}_i \tilde{u}_j}{\partial x_j} = - \frac{\partial \tilde{P}}{\partial x_i} + \nu \frac{\partial^2 \tilde{u}_i}{\partial x_j^2} + \frac{\partial \nu_e}{\partial x_j} \left(\frac{\partial \tilde{u}_i}{\partial x_j} + \frac{\partial \tilde{u}_j}{\partial x_i} \right), \quad (3.9)$$

where the tilde sign on the top of u and P represents the filtering operation. ν_e is the eddy viscosity defined by Vreman. The above two equations describe the mass and momentum conservation. The eddy viscosity is defined as:

$$\nu_e = c \sqrt{\frac{B_\beta}{\alpha_{ij} \alpha_{ij}}}, \quad (3.10)$$

where

$$\alpha_{ij} = \frac{\partial \tilde{u}_j}{\partial x_i}, \quad (3.11)$$

The symbol α_{ij} is a (3×3) matrix of derivatives of the filtered velocity \tilde{u} . Taking into account the machine precision error, according to Vreman, (2004), if $\alpha_{ij} < 10^{-8}$ or $B_\beta < 10^{-8}$, eddy viscosity ν_e is by definition zero. The coefficient B_β can be written as follows:

$$B_\beta = \beta_{11}\beta_{22} - \beta_{12}^2 + \beta_{11}\beta_{33} - \beta_{13}^2 + \beta_{22}\beta_{33} - \beta_{23}^2, \quad (3.12)$$

where

$$\beta_{ij} = \Delta_m^2 \alpha_{mi} \alpha_{mj}. \quad (3.13)$$

The filter width Δ_m equals to the cell size in the corresponding direction, e.g. $\Delta_1 = dx$ in x direction, $\Delta_2 = dy$ in y direction, and $\Delta_3 = dz$ in z direction. Only in case the filter width is homogeneous for all three directions, it can be assumed that $\Delta = dx = dy = dz$. The sub-index mi and mj represent summation operations. For example, the tensor β_{12} can be written as follows:

$$\beta_{12} = \Delta_1^2 \alpha_{11} \alpha_{12} + \Delta_2^2 \alpha_{21} \alpha_{22} + \Delta_3^2 \alpha_{31} \alpha_{32}. \quad (3.14)$$

The model constant $c \approx 2.5C_s^2$. It is proportional to the Smagorinsky constant C_s , which is approximately 0.1 for the turbulent channel flow with high Reynolds number, and 0.14 – 0.25 for isotropic turbulence. In the current simulation, $c = 0.07$ is adopted in order to keep the same with the channel flow validation by Vreman, (2004).

3.4. Discretization

The NS-equation is discretized on a three-dimensional Cartesian grid based on a staggered arrangement. In CaNS, the grid is by default uniform in x and y directions. In z direction, more flexibility is offered as Gauss elimination is used (see Costa, (2018)). The grid can be non-uniform in this direction. Users are free to adapt the grid resolution to their need.

A schematic of the top view of $x - y$ plane is shown in Figure 3.1. i and j denotes the index of the grid in x and y direction, and cell faces can be denoted as $i + \frac{1}{2}$ and $j + \frac{1}{2}$. Ghost points are created to tackle the boundary conditions. The distance between the ghost point and the cell face center equals to that between the cell face center the first cell center. All the cells in $x - y$ plane share the same size, including the boundary cells. In the context of three-dimensional models, the index of cell center is (i, j, k) . The corresponding x component velocity u is stored at cell east face center $(i + \frac{1}{2}, j, k)$, y component velocity v is stored at cell back face center $(i, j + \frac{1}{2}, k)$, and y component velocity w is at cell north face center $(i, j, k + \frac{1}{2})$.

One of the advantages of using staggered grid is that it avoids the velocity-pressure decoupling which is also referred to as checker-board problem. It has restricted the development of the collocated grid for decades until the use of Rhie-Chow interpolation Rhie and Chow, (1983). However, such interpolation brings a redundant kinetic energy dissipation term Tan and Huang, (2014). Therefore, using staggered grid could lead to more accurate results for simple geometries despite its incapability for applying to complex geometries, such as, curved structures. Additionally, using staggered grid requires large amount of careful interpolation, thus it is necessary to first introduce the detailed discretization of the composing terms in NS equation.

3.4.1. Velocity Gradient

As described in the previous section, velocity vectors are stored at the cell faces. Hence, velocity gradients are scalars and can be stored at cell centers. There are nine components of the velocity gradient. The simplest three are $\frac{\partial u}{\partial x}$, $\frac{\partial v}{\partial y}$, and $\frac{\partial w}{\partial z}$. $\frac{\partial u}{\partial x}$ is obtained by subtracting u at the east face (with

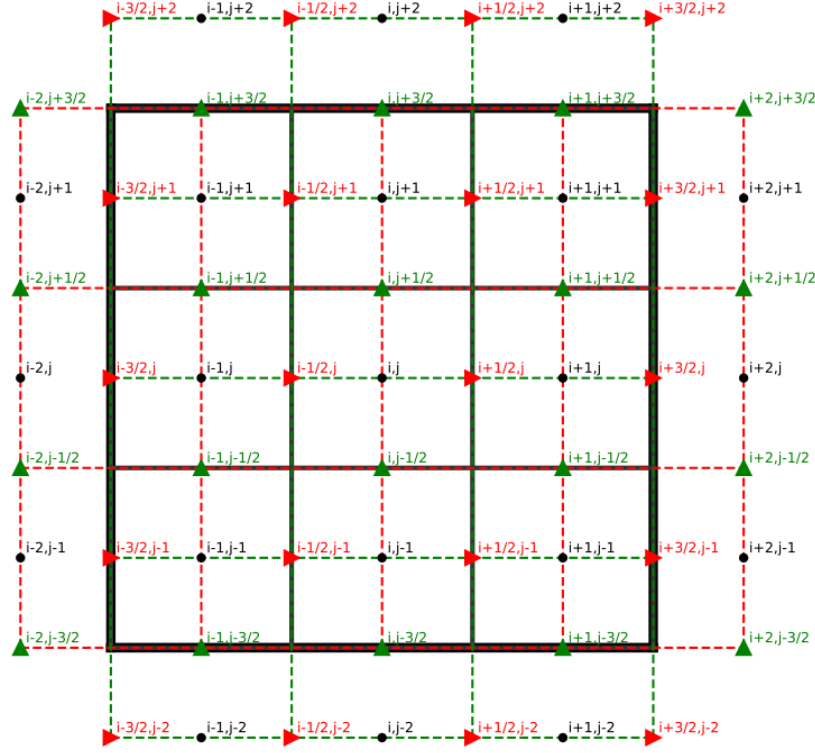


Figure 3.1: A 2D schematic of the staggered grid used by CaNS (top view). The thick solid lines represent the domain boundary and the thin solid lines are the boundaries of adjacent cells. The red triangles denote the location of velocity component u , the green triangles denote the location of velocity component v , and the black points are the cell centers including ghost cells. The green and red dashed lines suggest the staggered arrangement for u and v , respectively.

index $u(i, j, k)$ with u at the west face (with index $u(i - 1, j, k)$), and the difference is then divided by the local cell size in x direction dx . The derivation of the other two components is similar. Figure 3.2 demonstrates the velocity locations that are involved.

The interpolation for the rest of the velocity gradients is more complex but follows similar rules. Since the direct velocity gradient is not right at the cell center, but at the centers of four cell edges. The mean of them has to be taken as a more accurate value for the velocity gradient. An example is demonstrated using $\frac{\partial u}{\partial y}$. The schematic is shown in the picture a) in Figure 3.3. The four composing velocity gradients can be written as:

$$\frac{u(i, j + 1, k) - u(i, j, k)}{dy}, \quad \frac{u(i, j, k) - u(i, j - 1, k)}{dy}, \quad (3.15)$$

$$\frac{u(i - 1, j + 1, k) - u(i - 1, j, k)}{dy}, \quad \frac{u(i - 1, j, k) - u(i - 1, j - 1, k)}{dy},$$

corresponding to the point at east-back, east-front, west-back, and west-front vertical edge center. Because these four edge centers are the four closest to the present cuboid center, the interpolation can be obtained by taking the average of them as the velocity gradient value at the cell center. Similar rules apply to other components of the velocity gradient matrix, despite the difference is that the interpolating edges are different. For example, schematic b) in Figure 3.3 demonstrates the interpolation points for $\partial \tilde{u} / \partial z$.

The explanation for velocity gradient may seem unnecessary for the discretization of NS equation, however, the definition ensures the accuracy of the computation of the eddy viscosity in each cell, during which gradients play a crucial role. Higher order interpolation could also be conducted by involving more neighboring cells that are not directly adjacent to present cell. However, this puts higher demand for the computer power.

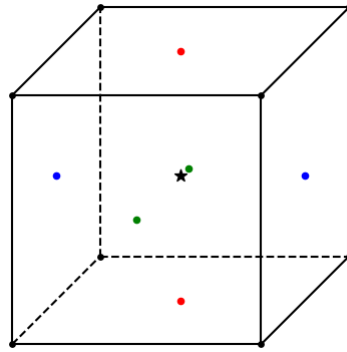


Figure 3.2: A schematic of the involved velocity locations for the derivation of velocity gradient. The cuboid demonstrates a computational grid cell. The blue points denote the location of u that are used to derive $\partial u/\partial x$. Similarly, green points are v locations that are for $\partial v/\partial y$, and red points are w locations and are for $\partial w/\partial z$.

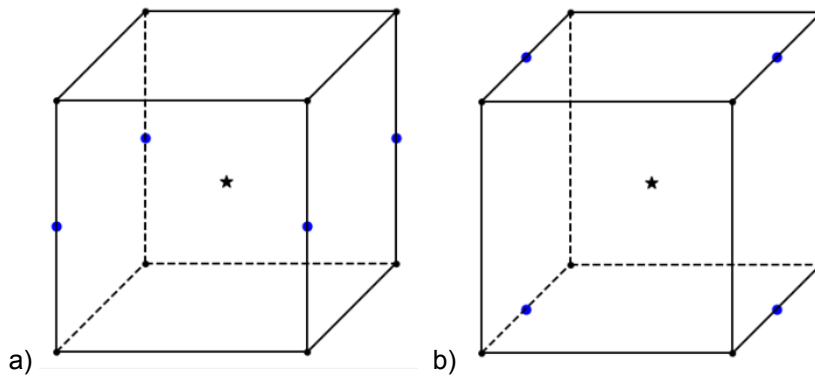


Figure 3.3: Schematics of the discretization of the velocity component $\frac{du}{dy}$ (shown in a)) and $\frac{du}{dz}$ (shown in b)). The blue points are the center of the edges, at which local velocity gradients are derived using the present and its adjacent cells. The four velocity gradients are then interpolated to obtain the value at the cell center marked by a black star.

3.4.2. Advection Term

The discretization of the NS equation is slightly different from the velocity gradient component, since either there are more than one single variable being differentiated or higher order of differentiation is needed. Hence, it would be straight forward to elaborate term by term.

First of all is the advection term, considering incompressibility and mass conservation, it can be written as:

$$\frac{\partial \tilde{u}_i \tilde{u}_j}{\partial x_j} \tag{3.16}$$

By taking x component momentum equation as an example, the following steps demonstrate how this term is discretized:

- $\frac{\partial \tilde{u}_i \tilde{u}_j}{\partial x_j}$ in x momentum equation can be expanded as :

$$\frac{\partial \tilde{u} \tilde{u}}{\partial x} + \frac{\partial \tilde{u} \tilde{v}}{\partial y} + \frac{\partial \tilde{u} \tilde{w}}{\partial z}, \tag{3.17}$$

assuming that they are term 1, 2, 3, respectively;

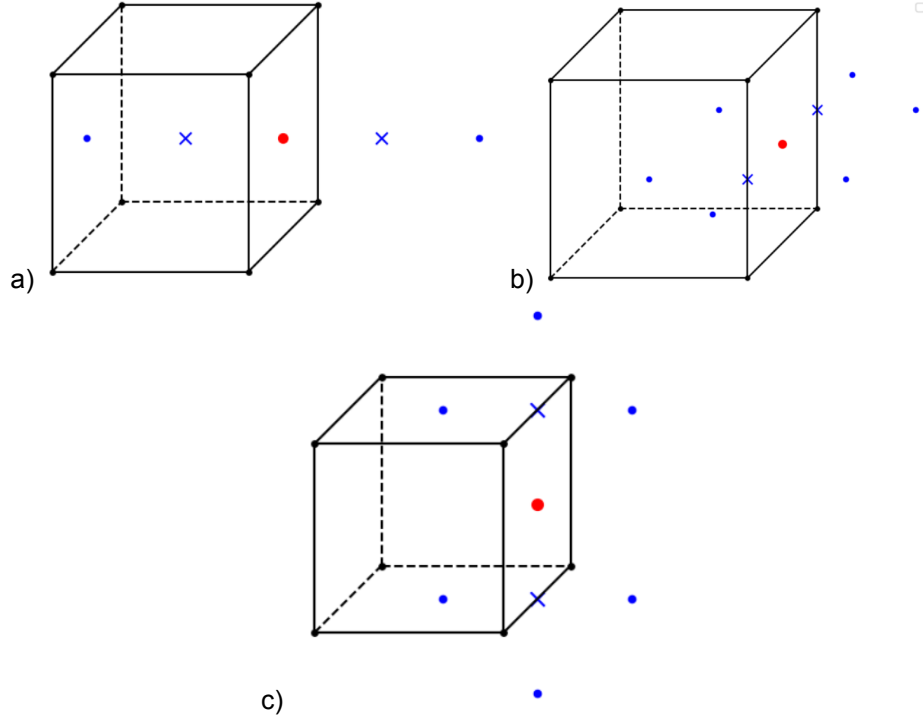


Figure 3.4: Schematics of the discretization for advection terms in x momentum equation, a) term $\partial\tilde{u}\tilde{u}/\partial x$, b) $\partial\tilde{u}\tilde{v}/\partial y$, and c) $\partial\tilde{u}\tilde{w}/\partial z$. The red dots represent the position where advection terms are evaluated, blue cross denote the locations of plus and minus terms in the differentiation, and the blue dots are the neighboring velocity points that are made use of.

- All these terms are evaluated at the corresponding velocity location. e.g. in x momentum equation it is at cell east face center. Similarly, for y momentum equation, it is at cell back face center, and for z momentum equation it is at cell north face center);
- A schematic is shown in Figure 3.4;
- Term 1 $\frac{\partial\tilde{u}\tilde{u}}{\partial x}$ may be differentiated as follows:

$$\begin{aligned} \left. \frac{\partial\tilde{u}\tilde{u}}{\partial x} \right|_{(i+0.5,j,k)} &= \frac{\tilde{u}\tilde{u}|_+ - \tilde{u}\tilde{u}|_-}{dx} \\ &= \frac{\frac{1}{2}[u(i+1,j,k) + u(i,j,k)] \times \frac{1}{2}[u(i+1,j,k) + u(i,j,k)]}{dx} \\ &\quad - \frac{\frac{1}{2}[u(i,j,k) + u(i-1,j,k)] \times \frac{1}{2}[u(i,j,k) + u(i-1,j,k)]}{dx}, \end{aligned} \quad (3.18)$$

the locations concerned are demonstrated in picture a) of Figure 3.4;

- Term 2 $\frac{\partial\tilde{u}\tilde{v}}{\partial y}$ can be expanded as:

$$\begin{aligned} \left. \frac{\partial\tilde{u}\tilde{v}}{\partial y} \right|_{(i+0.5,j,k)} &= \frac{\tilde{u}\tilde{v}|_+ - \tilde{u}\tilde{v}|_-}{dy} \\ &= \frac{\frac{1}{2}[u(i,j+1,k) + u(i,j,k)] \times \frac{1}{2}[v(i+1,j,k) + v(i,j,k)]}{dy} \\ &\quad - \frac{\frac{1}{2}[u(i,j-1,k) + u(i,j,k)] \times \frac{1}{2}[v(i-1,j,k) + v(i-1,j,k)]}{dy}, \end{aligned} \quad (3.19)$$

where $uv|_+$ is evaluated at the east-back edge center, and $uv|_-$ is evaluated at the east-front center, see picture b) of Figure 3.4;

- Similarly, term $3 \frac{\tilde{u}\tilde{w}}{\partial z}$ can be written as:

$$\begin{aligned} \left. \frac{\partial \tilde{u}\tilde{w}}{\partial z} \right|_{(i+0.5,j,k)} &= \frac{\tilde{u}\tilde{z}|_+ - \tilde{u}\tilde{z}|_-}{dz} \\ &= \frac{\frac{1}{2}[u(i,j,k+1) + u(i,j,k)] + \frac{1}{2}[w(i+1,j,k) + w(i,j,k)]}{dz} \\ &\quad - \frac{\frac{1}{2}[u(i,j,k-1) + u(i,j,k)] \times \frac{1}{2}[w(i+1,j,k-1) + w(i,j,k-1)]}{dz}, \end{aligned} \quad (3.20)$$

where $uw|_+$ is evaluated at the east-upper edge center, and $uw|_-$ is evaluated at the east-lower center, see picture c) of Figure 3.4.

3.4.3. Pressure Term

To be consistent with other quantities in the equation, the pressure gradient has to be also evaluated at the cell faces. In CaNS, pressure gradient is obtained by directly taking the gradient of the two neighboring cells. For example, the pressure term in x momentum equation can be written as:

$$\frac{\partial P}{\partial x} = \frac{P(i+1,j,k) - P(i,j,k)}{dx}, \quad (3.21)$$

where P is the total pressure.

3.4.4. Diffusion Term

In equation 3.9 the eddy viscosity introduces an extra diffusion term. However, the two diffusion terms can be merged and the momentum equation then becomes:

$$\frac{\partial \tilde{u}_i}{\partial t} + \frac{\partial \tilde{u}_i \tilde{u}_j}{\partial x_j} = -\frac{\partial \tilde{P}}{\partial x_i} + \frac{\partial}{\partial x_j} \left((v + v_e) \left(\frac{\partial \tilde{u}_i}{\partial x_j} + \frac{\partial \tilde{u}_j}{\partial x_i} \right) \right), \quad (3.22)$$

such that the two diffusion terms can be treated together, noting that one of the terms vanishes because of continuity:

$$v \frac{\partial^2 \tilde{u}_j}{\partial x_j \partial x_i} = v \frac{\partial^2 \tilde{u}_j}{\partial x_i \partial x_j} = v \frac{\partial}{\partial x_i} \left(\frac{\partial \tilde{u}_j}{\partial x_j} \right) = 0. \quad (3.23)$$

By substituting $(v + v_e)$ with total viscosity ν_t , the diffusion term can be expressed as:

$$\frac{\partial}{\partial x_j} \left((v + v_e) \left(\frac{\partial \tilde{u}_i}{\partial x_j} + \frac{\partial \tilde{u}_j}{\partial x_i} \right) \right) = \frac{\partial}{\partial x_j} \left(\nu_t \left(\frac{\partial \tilde{u}_i}{\partial x_j} + \frac{\partial \tilde{u}_j}{\partial x_i} \right) \right). \quad (3.24)$$

Discretizing such term again makes use of surrounding cells. x momentum equation is taken as an example, noting that all the terms have to be evaluated at the cell right face center. A schematic is shown in Figure 3.5.

- First, the diffusion term can be expanded as follows:

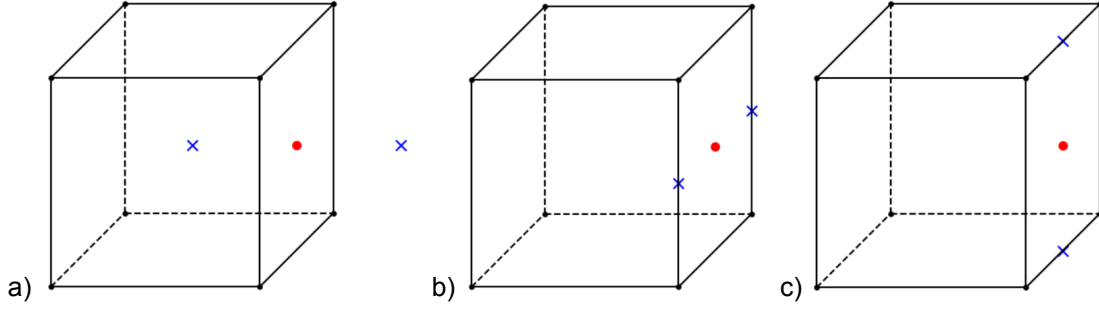


Figure 3.5: Schematics of the discretization for diffusion terms, taking x momentum equation as an example. a) term 1, b) term 2, and c) term 3, with blue crosses represent the location of the plus and minus terms in the differentiation as well as the targeted location of interpolation of eddy viscosity ν_e . Red dots are the location where the diffusion terms are evaluated.

$$\begin{aligned} \frac{\partial}{\partial x_j} \left(\nu_t \left(\frac{\partial \tilde{u}_i}{\partial x_j} + \frac{\partial \tilde{u}_j}{\partial x_i} \right) \right) &= \frac{\partial}{\partial x} \left(2\nu_t \frac{\partial \tilde{u}}{\partial x} \right) \\ &+ \frac{\partial}{\partial y} \nu_t \left(\frac{\partial \tilde{u}}{\partial y} + \frac{\partial \tilde{v}}{\partial x} \right) \\ &+ \frac{\partial}{\partial z} \nu_t \left(\frac{\partial \tilde{u}}{\partial z} + \frac{\partial \tilde{w}}{\partial x} \right), \end{aligned} \quad (3.25)$$

where they are again listed as term 1, term 2, and term 3;

- The discretization of term 1 makes use of the cell west and the cell east to the current one, written as:

$$\begin{aligned} \frac{\partial}{\partial x} \left(2\nu_t \frac{\partial \tilde{u}}{\partial x} \right) &= \left[\frac{\partial \tilde{u}}{\partial x} \Big|_{+} \nu_{t+2} - \frac{\partial \tilde{u}}{\partial x} \Big|_{-} \nu_{t-} \times 2 \right] \frac{1}{dx} \\ &= \left[2 \frac{u(i+1, j, k) - u(i, j, k)}{dx} \nu_t(i+1, j, k) \right. \\ &\quad \left. - 2 \frac{u(i, j, k) - u(i-1, j, k)}{dx} \nu_t(i, j, k) \right] \frac{1}{dx}, \end{aligned} \quad (3.26)$$

where the plus sign denotes the location of east cell center (e.g. cell $(i+1, j, k)$), and the minus sign points to the current cell center (e.g. cell (i, j, k)). These two locations coincide with where the eddy viscosity is located, thus there is no need to interpolate the eddy viscosity ν_e for this term;

- The term 2 may be written as:

$$\begin{aligned} \frac{\partial}{\partial y} \nu_t \left(\frac{\partial \tilde{u}}{\partial y} + \frac{\partial \tilde{v}}{\partial x} \right) &= \frac{1}{dy} \left[\left(\frac{\partial u}{\partial y} + \frac{\partial v}{\partial x} \right)_{+} \nu_{t+} - \left(\frac{\partial u}{\partial y} + \frac{\partial v}{\partial x} \right)_{-} \nu_{t-} \right] \\ &= \frac{1}{dy} \left[\frac{u(i, j+1, k) - u(i, j, k)}{dy} + \frac{v(i+1, j, k) - v(i, j, k)}{dx} \right] \nu_{t+} \\ &+ \frac{1}{dy} \left[\frac{u(i, j, k) - u(i, j-1, k)}{dy} + \frac{v(i+1, j-1, k) - v(i, j-1, k)}{dx} \right] \nu_{t-}, \end{aligned} \quad (3.27)$$

where the interpolation of the eddy viscosity can be obtained by taking the mean of ν_e at the four cell centers around the corresponding edge center, written as:

$$v_{t+} = \frac{1}{4} \left[v_t(i, j, k) + v_t(i+1, j+1, k) + v_t(i+1, j, k) + v_t(i, j+1, k) \right],$$

and

$$v_{t-} = \frac{1}{4} \left[v_t(i, j, k) + v_t(i+1, j, k) + v_t(i+1, j-1, k) + v_t(i, j-1, k) \right].$$

The plus and minus values are taken at the center of right-back and right-front edges, as shown in the schematic b) in Figure 3.5;

- Similarly, term 3 may be expressed as:

$$\begin{aligned} \frac{\partial}{\partial z} v_t \left(\frac{\partial \tilde{u}}{\partial z} + \frac{\partial \tilde{w}}{\partial x} \right) &= \frac{1}{dzf(k)} \left[\left(\frac{\partial u}{\partial z} + \frac{\partial w}{\partial x} \right)_+ v_{t+} - \left(\frac{\partial u}{\partial z} + \frac{\partial w}{\partial x} \right)_- v_{t-} \right] \\ &= \frac{1}{dzf(k)} \left[\frac{u(i, j, k+1) - u(i, j, k)}{dzc(k)} + \frac{w(i+1, j, k) - w(i, j, k)}{dx} \right] v_{t+} \\ &+ \frac{1}{dzf(k-1)} \left[\frac{u(i, j, k) - u(i, j, k-1)}{dzc(k-1)} + \frac{w(i+1, j, k-1) - w(i, j, k-1)}{dx} \right] v_{t-}, \end{aligned} \quad (3.28)$$

where dzf is cell size and dzc is cell center spacing. Since the grid is not uniform in z direction, $\frac{1}{4}$ can not be used to approximate v_{t+} and v_{t-} . Linear interpolation can be utilized to obtain the eddy viscosity at edge centers.

3.5. Signed Distance Field

Signed Distance Field (SDF) is used in the solver to represent complex shape of geometries. SDF is the orthogonal distance of a given point to its nearest boundary in a metric space, with the sign determined by whether the point is inside or outside of the geometry. In the current research, SDF can be computed using a novel code named "STL2SDF". "STL2SDF" uses '.stl' or '.obj' source files that represent structure boundary, and computes the SDFs based on the computational grid generated by CaNS. The signed value is negative when the point is inside of the structure boundary and positive when outside. The signed distance approaches zero when the grid point gets closer to the boundary. Due to the use of Immersed Boundary Method, the boundary of the structure is immersed in the computational grid. Without SDF, the solver cannot identify the location of the boundary. SDF is easy to implement in CaNS and can clearly indicate the distance between the grid node and the boundary, therefore different grid points can be tackled differently by the IBM.

Because of the staggered arrangements of velocity components, STL2SDF generates three SDFs, for u , v , and w , which are the input files for the solver. p location SDF is later reconstructed by interpolation. When using the STL2SDF, the number of sample points needs to be sufficiently large in order to accurately capture the boundary. It is very case sensitive, and thus its results need to be examined by either isosurfaces or 2D slices. The workflow of generating the SDF files may be simply concluded as:

- Simple geometry operations, such as, rotation, translation, scaling can be applied by "STL2SDF", making it easy to adjust the geometry according to user need;
- The '.obj' or '.stl' files can be either from external resources or easily generated by 3D modeling software, such as Gmsh;
- the structure surfaces have to be watertight, which means that the structure is sufficiently closed. Otherwise, the computed SDFs may face a "leaking" problem. The leaking problem comes from the fact that with an unclosed surface the program give wrong signed distance value at a set of certain coordinates;
- "STL2SDF" computes the SDFs and converts them into binary files that can be read by CaNS.

3.6. Immersed Boundary Method

A stair-step Immersed Boundary Method (IBM) is used to tackle the complex structure boundary. A schematic is shown in Figure 3.34. Generally, the grid points can be classified into three categories: solid points, fluid points, and forcing points. The solid points are the grid points in the solid phase within the obstacle boundary, and fluids points are the grid points within the fluid domain. Forcing points are the those in the fluid domain but directly next to the interface. With the stair-step IBM, the interface is roughly represented by the cuboid grid structure. The effect of the obstacle can be interpreted as an added force to the forcing points. This can be written by:

$$u_i^k = u_i^* + \Delta t f_i^k, \quad (3.29)$$

where the f_i is the added IBM force, and u_i^* is the prediction velocity that is the same in the RK3 scheme, $u_i^* = u_i^{k-1} + \Delta t RHS_i^k$. With the stair-step IBM, it can be assumed that the interface perfectly coincides with the corresponding velocity location. As a result, the left hand side of equation 3.29 can be assumed equal to velocity at the boundary. Therefore, the IBM force can be expressed as:

$$f_i^k = \frac{u_{b,i} - u_i^*}{\Delta t}. \quad (3.30)$$

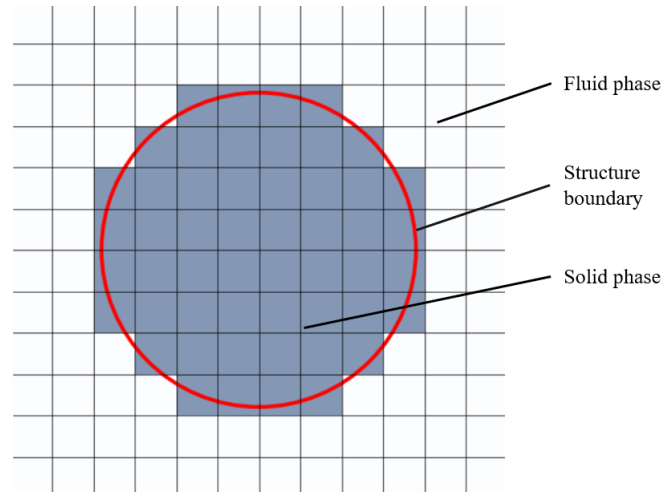


Figure 3.6: A 2D schematic of the stair-step IBM. The white area represents fluid domain, the red line is the structural boundary, and the blue area represents the approximated obstacle. When the boundary encloses more than half of the boundary cell, then the cell is approximated as solid phase.

The stair-step is easy to implement, however, blurs the curved structure boundary into a mosaic-like pattern and thus decreases the computation accuracy, especially for the geometries with sharp and curved edges. Considering future development of the program, such issues can be tackled by using Yang and Balaras IBM (see Yang and Balaras, (2006)).

Yang and Balaras IBM can more accurately obtain the forcing of the boundary points by interpolation using extra points. Figure 3.7 shows a schematic of 2D IBM interpolation. In the 3D case, three different interpolation points are needed. When sufficiently close to the interface, a linear relationship can be assumed between any variable ϕ and its position as follows:

$$\phi = b_1 + b_2x + b_3y + b_4z, \quad (3.31)$$

where the point 1 represent the point on the boundary, and 2-4 are the interpolation points. The coefficients $b_1, b_2, b_3,$ and b_4 can be computed from the following system of equations:

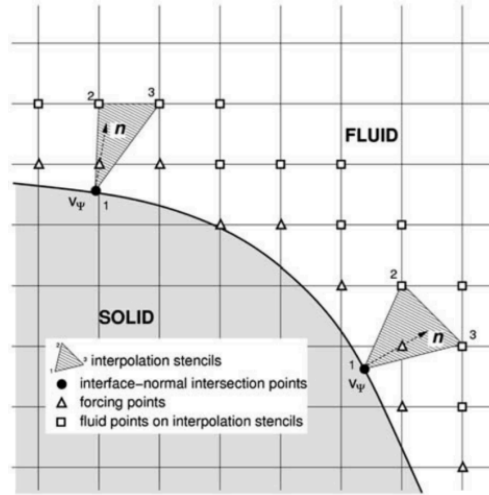


Figure 3.7: Yang and Balaras IBM, interpolation in 2D. The squares are the fluid point and the triangles are forcing points. The two gray triangle areas are two examples for the interpolation point and the n arrows are the boundary local normal direction (taken from Yang and Balaras, (2006)).

$$\begin{bmatrix} b_1 \\ b_2 \\ b_3 \\ b_4 \end{bmatrix} = A^{-1} \begin{bmatrix} \phi_1 \\ \phi_2 \\ \phi_3 \\ \phi_4 \end{bmatrix} = \begin{bmatrix} 1 & x_1 & y_1 & z_1 \\ 1 & x_2 & y_2 & z_2 \\ 1 & x_3 & y_3 & z_3 \\ 1 & x_4 & y_4 & z_4 \end{bmatrix}^{-1} \begin{bmatrix} \phi_1 \\ \phi_2 \\ \phi_3 \\ \phi_4 \end{bmatrix} \quad (3.32)$$

where (x_1, y_1, z_1) , (x_2, y_2, z_2) , (x_3, y_3, z_3) , and (x_4, y_4, z_4) are the four points in the interpolation stencil. Thus, the variable at the boundary point may be written as:

$$\phi^{interp,f} = [1 \quad x^{interp,f} \quad y^{interp,f} \quad z^{interp,f}] b^T. \quad (3.33)$$

Substituting the variable with velocity, at the forcing points, the forcing can be computed as follows:

$$f_i = \frac{u^f - u^{interp,f}}{\Delta t}, \quad (3.34)$$

where u^f is the velocity at the forcing point, and $u^{interp,f}$ is the interpolated velocity.

Channel Flow Validation

This chapter describes the first stage, turbulent channel flow (TCF) validation. The reason for using TCF lies in its simple geometry, fast and easy flow setup, as well as the large amount of numerical and experimental data available for comparison. The validation data not only include bulk mean parameters, as well as more elaborate statistics such as the first and second-order moments of flow velocity and pressure, for example, mean velocity profile and Reynolds stress tensor. The former could give a general overview of the correctness of the TCF setup, and the latter gives more details and insights into the validation, for example, dissipation profile. In this stage, various parameters are computed and compared to validate the LES, including mean velocity, turbulent intensities, eddy viscosity, and Reynolds shear stress.

4.1. DNS Validation

Pressure-driven turbulent channel flow has been validated by Costa, (2018) using CaNS by Direct Numerical Simulations (DNS). The size of the channel is $L_x \times L_y \times L_z = 6 \times 3 \times 1$ with a uniform computation grid having dimension $N_x \times N_y \times N_z = 512 \times 256 \times 144$ in each direction. Periodic boundary conditions are applied in both streamwise and spanwise directions, and the channel walls are assumed no-slip. The Reynolds number is $Re = 5640$, based on bulk velocity and full channel height. A vortex pair according to Henningson and Kim, (1991) along the streamwise direction is added in order to facilitate transition to turbulent regime. Figure 4.1 shows the obtained streamwise mean velocity and the turbulence intensity. The friction Reynolds number is $Re_\tau = 180$, agreeing excellently with the comparison data from Kim et al., (1987).

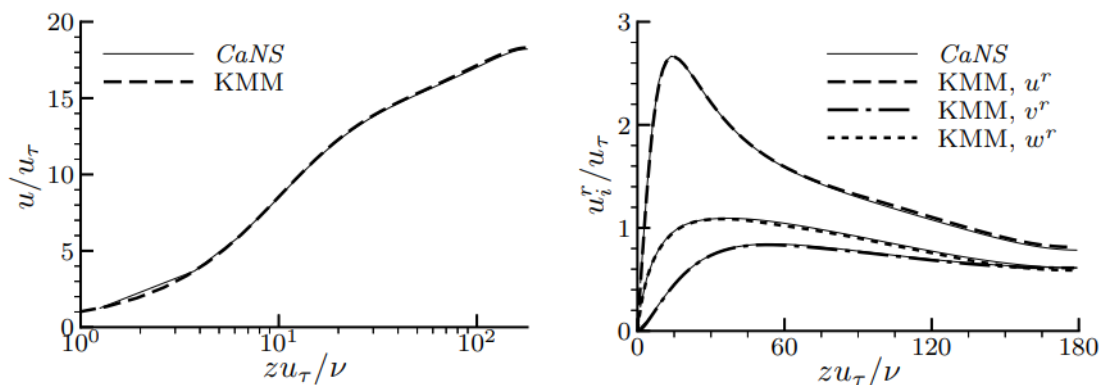


Figure 4.1: Turbulent intensities of the turbulent channel flow with $Re_\tau = 180$, taken from Costa, (2018).

The good agreement shows that CaNS code is sufficiently accurate for turbulent channel flows by using DNS. Based on this, LES can be implemented using similar grid. In Vreman model, the computation

grid itself functions as a filter. The eddies larger than the filter width contain most of the turbulent kinetic energy (TKE) and are explicitly resolved. The smaller subgrid-scale (SGS) scales are filtered out by the filter but subsequently modeled by the eddy viscosity model. One advantage of this is that the computation of the flow with higher Reynolds number that possibly exceeds the ability of DNS can be achieved. Given the same degree of freedom with DNS, LES can compute the flows with either higher velocity or larger characteristic length scale, since LES does not require a mesh as fine as DNS.

4.2. LES Validation

A turbulent plane Poiseuille flow similar with DNS validation is used for the current step. The flow is driven by a constant pressure gradient. The purpose of this step is to validate the correctness of the LES implementation. Fortunately, Vreman, (2004) contains the validation with TCF for its own model, as well as its comparison with DNS and Smagorinsky and dynamic Smagorinsky model. The focus of the current study is to assure that the Vreman model is properly inserted into CaNS rather than the preciseness of Vreman model itself compared with other eddy viscosity models under a same discretization scheme. Thus, the results of Smagorinsky and the dynamic Smagorinsky are skipped, and only Vreman's well as DNS data from Vreman, (2004) are compared.

4.2.1. Flow Setup

In this section the TCF setup is introduced. The channel has a dimension of $6H \times 2H \times 2H$ in x, y , and z direction, where H is the half channel height and is assumed 1 in the simulation for simplicity. x and y directions are streamwise and spanwise directions, respectively. Periodic boundary conditions are posed in these directions. Along z direction, both the lower and upper boundaries have no-slip walls, and the flow cannot penetrate the walls. Identical with the grid used by Vreman, (2004), the grid has $N_x \times N_y \times N_z = 47 \times 47 \times 63$ degrees of freedom, with uniform spacing in x and y direction. Along z coordinate, the grid is finer at the boundaries and coarser at channel center, and the location of the fifth cell center is at $y^+ = 11$. By using the relation $y^+ = Re_\tau y$, the actual location is $y = \frac{y^+}{Re_\tau} = \frac{11}{360} \approx 0.030556m$. The grid in z direction is generated with a grid generation function:

$$zf(k) = \frac{1}{2} \left[1 + \frac{\tanh\left(\frac{k}{N_z} - 0.5\right)gr}{\tanh(gr/2)} \right], \quad (4.1)$$

where zf_k defines the coordinate of the upper face of each cell, k is the index of the grid node, and gr is the growth ratio for the function.

The friction Reynolds number is $Re_\tau = 360$, based on the friction velocity u_τ , half channel height H and normal viscosity ν . In CaNS, for the pressure-driven flows two parameters can be tuned to satisfy a predefined friction Reynolds number, the pressure gradient $\partial P/\partial x$ and the viscosity ν . For simplicity's sake, the half-channel height is set to $H = 1$. Although the exact values of fluid viscosity and pressure gradient may not have a direct connection to a real application, the crucial dimensionless number Reynolds number is kept identical with Vreman, (2004), such that the results can be indicative of characteristics of flow with actual viscosity, such as water and air flow. For ease of reproducibility, the detailed flow setup is computed and listed below:

- The relation $Re_\tau \approx 0.09Re^{0.88}$ describe by Pope, (2001) is used to estimate the bulk Reynolds number of the flow. By taking $Re_\tau = 360$, the estimated Reynolds number

$$Re = \left(\frac{Re_\tau}{0.09} \right)^{\frac{1}{0.88}} = \left(\frac{360}{0.09} \right)^{\frac{1}{0.88}} \approx 12395;$$

- Assuming the bulk flow velocity equals to $U_{bulk} = 1m/s$, fluid viscosity is obtained $\nu = 1.6136^{-1}m^2/s$;
- Although the kinematic viscosity is significantly different from water or air, the corresponding friction Reynolds number $Re_\tau = 360$ is the same with Vreman, (2004);

- The friction velocity is $u_\tau = 0.0581\text{m/s}$, and the pressure gradient is $-\frac{\partial p}{\partial x} = \frac{u_\tau^2}{L_z} = 0.003374\text{Pa/m}$, assuming fluid density unity;
- The pressure gradient and viscosity function are the input for CaNS.

The initial condition is implemented by prescribing a mean flow profile with the $U_z = U(z/H)^{1/7}$, with 5% noise added and a streamwise vortex same with that in the DNS validation (Henningson and Kim, (1991)) is also applied to facilitate the transition, since the added noise may not be enough to trigger transition for TCF.

4.3. Results

The eddy turn over time T_e can be computed as

$$T_e = \frac{H}{u_\tau} = \frac{1}{0.0581} = 17.2\text{s}.$$

According to Vreman, (2004), the statistics was averaged from $10T_e$ to $30T_e$. In the present study, a longer averaging period is used, which is roughly from 200s to 1000s , around $11T_e$ to $58T_e$. The code iterated for 50000 steps. Time, forces, and bulk mean data data are outputted every 10 steps.

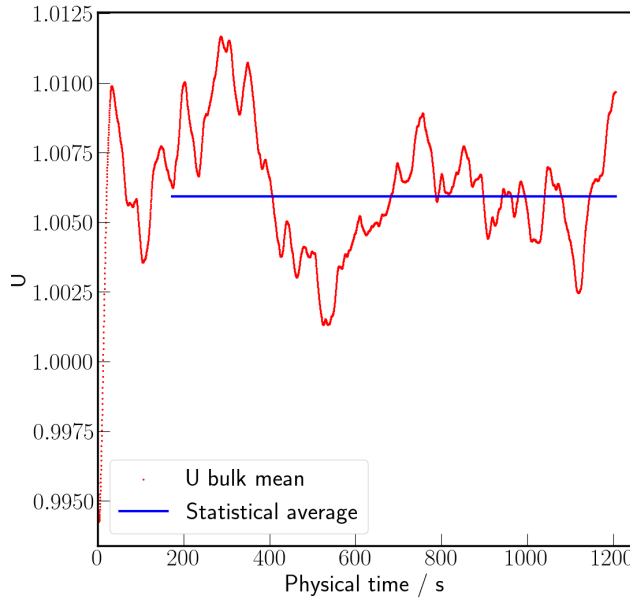


Figure 4.2: Bulk mean velocity of turbulent channel flow. The red dots are the bulk mean velocity of each output time step, and the red line is the time averaged bulk velocity.

Figure 4.2 shows bulk mean velocity as a function of time. In the code, the bulk mean velocity is obtained by summing up the cell local velocities multiplied by grid volume ratio. From the figure, although the fluctuations appear large, they are actually no large than 1.2% deviation from the mean value. When a constant pressure gradient is applied, streamwise bulk mean velocity fluctuates with time because of the presence of eddies as an inherent nature of turbulence.

Figure 4.3 shows the mean streamwise velocity profile and the Vreman eddy viscosity profile along z direction. From a) it can be observed that the bulk velocity profile generally agrees well with the data from Vreman, (2004). In b) near the wall at $y^+ \leq 25$, the eddy viscosity values agree excellently. When getting farther away from the wall, it may appear strange that the eddy viscosity values from validation's deviate from that of Vreman. However, eddy viscosity may not be a perfect parameter to examine the accuracy of the results. As can be seen from equation 3.10 and 3.13, eddy viscosity ν is

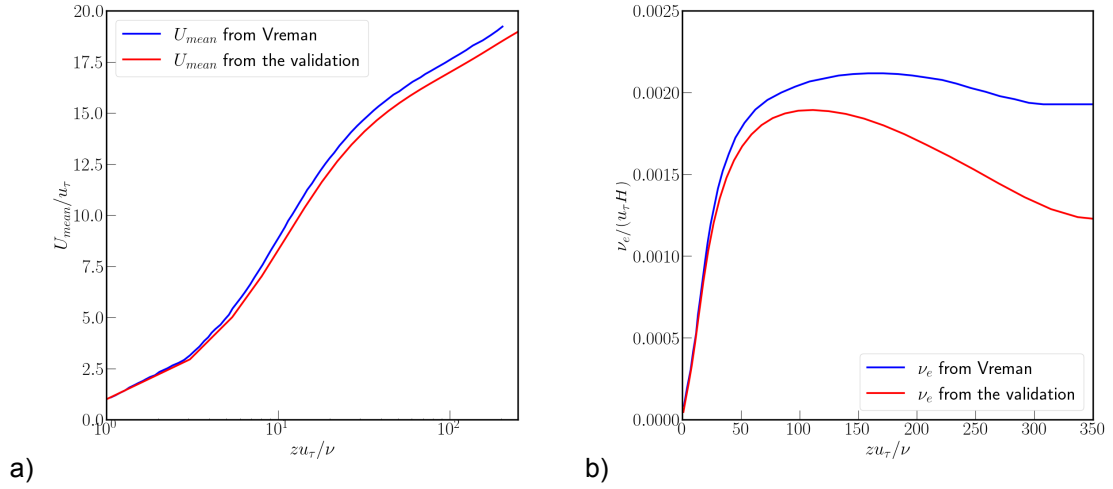


Figure 4.3: Mean velocity profile and eddy viscosity ν_e profile of Vreman model as a function of zu_{τ}/ν , a) plan-form averaged velocities, and b) plan-form averaged eddy viscosity ν_e . In both plots, the blues line are the comparison data from Vreman, (2004), and the red lines are the results from the current validation.

highly dependent on the grid size. At the grids near the wall, since the 5th grid center coordinate is kept at $y^+ = 11$, same was done by Vreman, (2004). The size of the cells near the wall could be similar with Vreman's. This could reasonably explain why the two eddy viscosity profiles agree excellently well when $y^+ \leq 25$. However, it is inspected that different grid generation functions are used for the two studies compared above. Thus, the grid spacing could be greatly different in the logarithmic law region as well as in bulk flow region. As a result, the eddy viscosity values are different. Additionally, numerical discretization are adopted by the two studies, the errors stem from this could also contribute to the discrepancy. It is certain that more turbulence characteristics need to be checked in order to provide more solidified validation for the code.

In LES, corrected turbulence quantities consist two parts, the first part may be called resolved part which represents large eddies that contain most of the turbulent kinetic energy and is explicitly resolved by the filter. The other part can be called unresolved part which represents the characteristic of subgrid scales and has to be modeled. Figure 4.4 shows the comparison of total dissipation and the SGS dissipation. The SGS dissipation is evaluated using the expression stated in Vreman, (2004):

$$\begin{aligned} \langle \nu_e |S|^2 \rangle &= \langle \nu_e 2||S||^2 \rangle = \langle \nu_e 2S_{ij}^2 \rangle \\ &= \langle 2\nu_e (S_{11}^2 + S_{22}^2 + S_{33}^2 + 2S_{12}^2 + 2S_{13}^2 + 2S_{23}^2) \rangle, \end{aligned} \quad (4.2)$$

where the symbol $\langle \rangle$ represents the spatial average along the statistically homogeneous directions x and y . $|S|$ is the rate of strain and equals to $\sqrt{2||S||^2}$. S_{ij} is defined as $S_{ij} = (\partial u_i / \partial x_j + \partial u_j / \partial x_i)$. The total dissipation is the summation of SGS dissipation and the resolved dissipation. The resolved dissipation is obtained by using the relation from Vreman, (2004):

$$\langle \nu |S'|^2 \rangle = \langle \nu 2S_{ij}'^2 \rangle = \langle \nu 2(S_{ij} - \langle S_{ij} \rangle) \rangle, \quad (4.3)$$

In the code, this term is obtained by first getting the $x - y$ planform average to reach $\langle S_{ij} \rangle$. Then in each cell, local S_{ij} is subtracted by $\langle S_{ij} \rangle$, and then the difference is planform-averaged again such that $\langle S_{ij}' \rangle$ is obtained. Subsequently, this value is multiplied by the fluid viscosity, which is assumed a constant, to get the resolved part of dissipation.

From Figure 4.3, SGS dissipation of the validation agrees well with Vreman's results. As for the corrected dissipation, the current validation result is slightly lower than the results from Vreman, (2004)

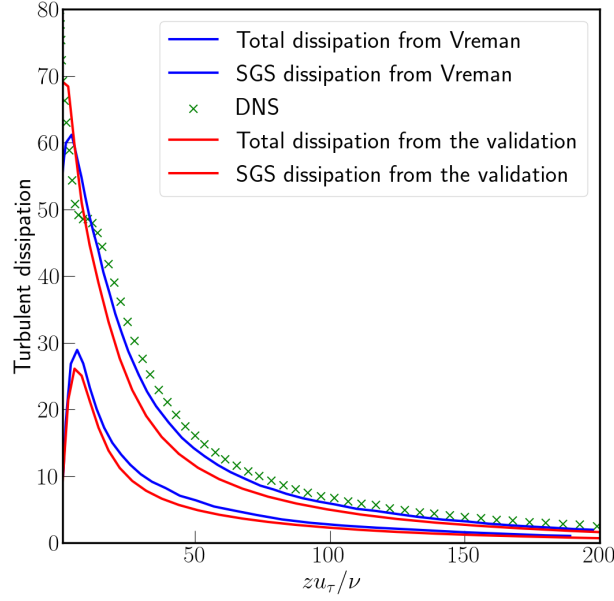


Figure 4.4: Profile of planform averaged Dissipation for Turbulence Channel Flow validation. The blue lines are the total and SGS dissipation from Vreman, (2004), green crosses are the DNS data from HU and Sandham, (2001), and red lines are the results from the current validation. The dissipation is normalized by u_τ^3/H .

in the buffer layer ($5 \leq y^+ \leq 50$) and logarithmic region ($50 \leq y^+ \approx 125$). Corrected dissipation decreases to zero at the center of the flow where shear production and transport also vanish. In the viscous sublayer ($y^+ \leq 5$), where the dissipation is merely compensated by viscous transportation, the current study achieves closer results to DNS, and the dissipation increases when closer to the wall, whereas the dissipation from Vreman, (2004) has a small dip at the wall. In general, the results from the current validation achieve good agreement with the reference.

One of the reasons contributing to the discrepancy could be that the two studies use different discretization schemes. Although the terms in the NS equation are discretized using a similar approach, Vreman, (2004) uses a collocated grid whereas the present work adopts a staggered grid. The discrepancy could possibly also stem from the errors of the numerical discretization. Additionally, with finite difference method, collocated arrangement is believed to generate slightly more numerical dissipation than the staggered arrangement Moin and Mahesh, (1998). The reason could be that when using collocated grid, one needs to avoid the checkerboard problem by applying velocity-pressure coupling method through adding an extra term, which indirectly adds as a source term for the turbulent kinetic energy (see Tan and Huang, (2014)). However, the proportion of numerical dissipation to the total dissipation is small, and the major contribution is from the viscous and SGS dissipation, which stem from the viscous diffusion term and eddy viscosity term, respectively.

Figure 4.5 shows the planform average of the resolved and corrected turbulent intensity, and Figure 4.6 are the resolved and corrected Reynolds stress $\overline{u'w'}$. The resolved turbulent intensities are obtained by using the RMS (Root Mean Square) of the fluctuation component, this can be written by the following relation:

$$\text{Turbulent intensity} = \frac{\sqrt{\langle u'^2 \rangle}}{u_\tau^2} \quad \frac{\sqrt{\langle v'^2 \rangle}}{u_\tau^2} \quad \frac{\sqrt{\langle w'^2 \rangle}}{u_\tau^2} \quad . \quad (4.4)$$

In CaNS, the square of the fluctuation is obtained by Reynolds decomposition $\langle u'^2 \rangle = \langle u^2 \rangle - \langle u \rangle^2$, and

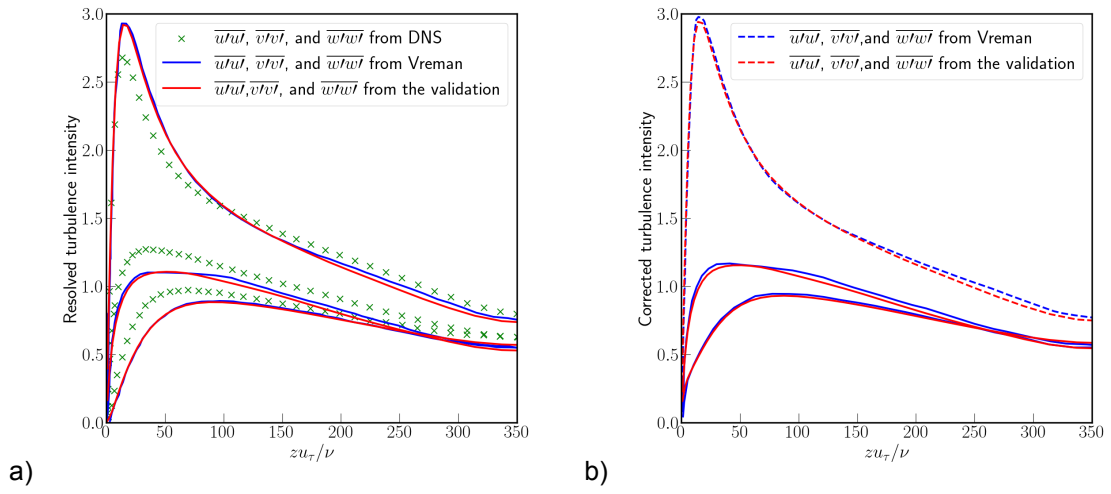


Figure 4.5: Plan-form averaged resolved and corrected turbulence intensity, a) the resolved turbulence intensity, b) turbulence intensity. In both plots, the line on the top is $\overline{u'w'}$, at the middle is $\overline{w'w'}$, and at the bottom is $\overline{v'v'}$.

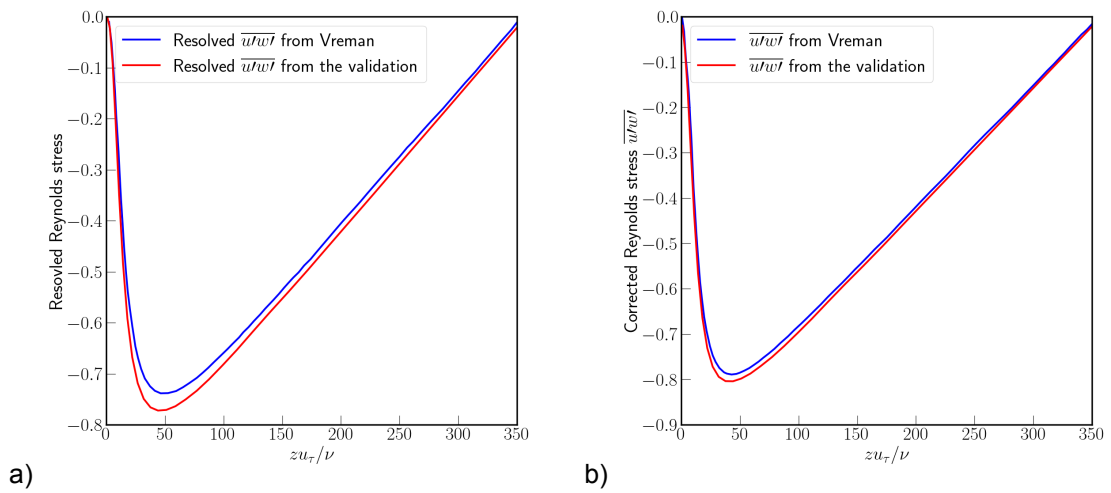


Figure 4.6: Plan-form averaged resolved and corrected Reynolds stress $\overline{u'w'}$, a) resolved and b) corrected.

the data is outputted every 10 time steps. Time average is taken subsequently. According to Vreman, (2004), the unresolved Reynolds stress tensor can be obtained with the formula:

$$\left\langle 2\nu_e S_{ij} + \frac{2}{3}k_\tau \delta_{ij} \right\rangle, \quad (4.5)$$

where the $k_\tau = 2\nu_e |S|$.

From the two figures it can be observed that the validation results agree well with that from Vreman, (2004). In Figure 4.5, the results agree perfectly with the reference data when $y^+ \leq 75$. In the region $y^+ \geq 75$, the present validation has turbulence intensity only slightly smaller than the data from Vreman, (2004), however, the discrepancy could be neglected because the error ratio is small. In Figure 4.6, the validation also shows generally good agreement with the reference data, especially good alignment can be found at $y \leq 25$. The absolute value of the validation's Reynolds stress is smaller than that from the reference at around $y^+ = 50$, this could also be reasonably explained by the error that originated from the different discretization.

5

Flow Over Cube Array Validation

In the previous chapter the turbulent channel flow validation has achieved excellent agreement with the reference data from Vreman, (2004), indicating the good implementation of the Vreman LES model in CaNS. Subsequently, this chapter concerns further implementation of Immerse Boundary Method (IBM). With IBM, the obstacle boundary is immersed into a simple computational grid that could be easily generated with CaNS. Signed-Distance Field (SDF) is computed and functions as a convenient medium to identify the location of the boundary, allowing for the IBM to further easily classify the grid points according to the phase they are situated. A stair-step IBM is used for the current stage, it approximate the shape of the interface using cells and then models the effect of the boundary as an added force for the points next to the interface.

5.1. Introduction

In this chapter, flow over periodic cube arrays is adopted as a validation for the IBM implementation. On of the advantage of using such geometry is that large amount of previous experiment and simulation data are available for comparison. Wind tunnel measurement and DNS data are available in the work by Castro et al., (2006) and Coceal et al., (2006). Fortunately, one of the previous researches done by Tomas et al., (2016) includes LES data. His work mainly concerns the roughness transition and periodic roughness over cubic arrays, however, Vreman model implemented in the LES code named DALES (Dutch Atmospheric Large-Eddy Simulation) has been firstly validated against wind tunnel measurement data from Castro et al., (2006). To the interest of the present study, the geometry used by Tomas et al., (2016) becomes a perfect example for the present validation, in which the same LES eddy viscosity model is used.

A schematic of the geometry is shown in the Figure 5.1. Similarly with the work by Tomas et al., (2016), the white region is adopted as the simulation region also in the study. The dimension of the flow domain is $4h \times 4h \times 10h$, where h is the height of each cube. Two periods of arrays are used in both streamwise and spanwise directions such that large eddies can be sufficiently tracked. $10h$ is the vertical extent of the domain such that roughness sublayer and the inertial sublayer can be modeled sufficiently, which could possibly extent to height of $1.5h$ and $2.3h$, respectively, according to Castro et al., (2006).

5.2. Flow Setup

The flow setup again may not have direct connection to a real application in terms of fluid kinematic viscosity and pressure gradient, however, the dimensionless Reynolds number is kept the same, allowing for the indirect implication through Reynolds similarity. In this case, the cube height is set to $h = 1m$, and the inverse of the viscosity is kept to $6197.5s/m^2$. The friction velocity based Reynolds number is $Re_\tau = 371$. Hence, the friction velocity can be computed as

$$u_\tau = \frac{Re_\tau \nu}{h} = \frac{371}{6197.5} m/s = 0.059863 m/s. \quad (5.1)$$

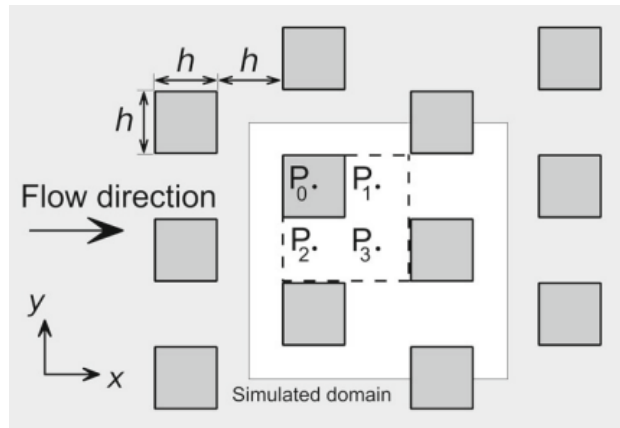


Figure 5.1: A schematic of the flow domain of the LES validation case from Jasper Tomas et al., (2016) (The figure is taken from Tomas et al., (2016)). The white region is the $4h \times 4h$ simulated area consisting of two periods of cube arrays. The cube dimension is $h \times h \times h$. The grey area represents the staggered arrangement of cube arrays in the previous wind tunnel experiment by Castro et al., (2006). P1 to P4 marks the location of line probes, on which the turbulence statistics are sampled.

Consequently, the velocity gradient can be expressed as:

$$\frac{dp}{dx} = \frac{u_\tau^2}{L_z} = \frac{0.059863^2}{10} = 0.00035836 Pa/m, \quad (5.2)$$

where L_z is the flow domain size in z direction, assuming density unity. The flow is again added with 5% noise in all directions to facilitate the transition to turbulent flow. Nonetheless, the streamwise wall turbulence vortex pair is not needed for this validation since the cubes are hydrodynamically rough (see Raupach et al., (1991)) and transition can be naturally triggered.

A computational grid similar with the one used by Tomas et al., (2016) is adopted for the validation. The grid dimension is $N_x \times N_y \times N_z = 64 \times 80 \times 112$. The canopy height equals to the cube height $h = 1$. Along z direction, 28 grid cells are uniformly spaced within the canopy. Above the canopy, the smallest spacing is $0.028h$ at the top of the cube. The grid stretches with increasing z coordinate. A grid generation function different with the channel flow validation is used, with the larger spacing on the top of the flow domain:

$$zf_k = 1 \left[1 + \frac{\tanh\left(\frac{k}{N_z} - 1\right)gr}{\tanh(gr)} \right], \quad (5.3)$$

with which the generated grid volume growth rate never exceeds 1.04.

Identical to the grid resolution achieved by Tomas et al., (2016), both validations are wall-resolved, and no wall function is needed. For a wall-resolved LES, although recommended, the $y^+ = 1$ criteria is not necessarily to be satisfied. The study by Tomas et al., (2016) covers each cube with $16 \times 20 \times 28$ grids and reasonably claims that such resolution can achieve a sufficient wall resolved LES, based on the fact that even coarser grids have been studied and proven satisfactory. According to Kanda et al., (2004), $10 \times 10 \times 10$ is adequate to explicitly resolve the cube roughness, and W.-C. Cheng and Porté-Agel, (2015) uses $10 \times 10 \times 15$ to cover each cube. Although, it would be found later that on the top of the cube arrays the grid did not simulate the shear layer precisely, it is sufficient for the major purpose of the current stage, to validate the IBM part in CaNS code.

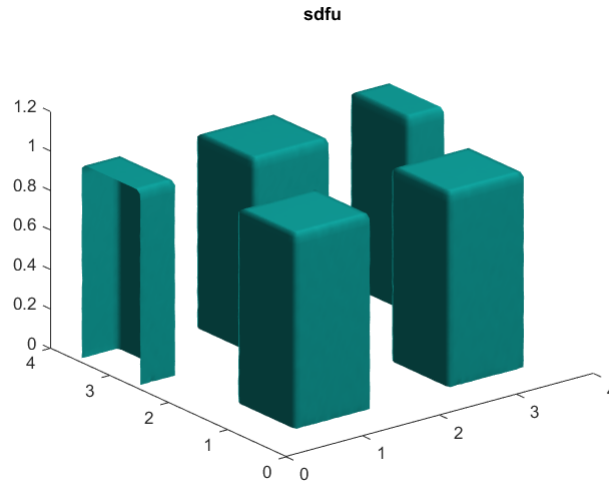


Figure 5.2: An isosurface of the SDF of u coordinate for the cube array validate case generated with MATLAB.

5.3. Results

SDF is convenient for bridging the object geometry with the IBM, and is computed firstly.

In Figure 5.2, the isosurface generated using MATLAB for the SDF of u location. It can be seen that the cube geometry is well-represented. The isosurface provides a general overview of the SDF, in order to minimize the interpolation and the grid rendering error by the isosurface function in MATLAB. Sliced views are shown in Figure 5.3. As can be observed, the boundary of the cube arrays are clearly indicated by the black lines in both $x-y$ plan and $x-z$ plane. The interior of the cubes have negative signed distance values, and the outside has positive values. The absolute value of signed distance becomes higher as the distance to the boundary larger, this is also indicate by the iso-contour in the slices. It can be demonstrated that the obstacle boundary can be sufficiently processed through "STL2SDF", which is thus applicable to CaNS with IBM.

The simulation runs for a total of 400000 iterations, and CFL number is limited to no greater than 0.95. The eddy turnover time based on the roughness height can be computed as:

$$T_e = \frac{h}{u_\tau} = \frac{1}{0.059863} \approx 16.7s, \quad (5.4)$$

where $h = 1m$ and u_τ is the friction velocity. Flow reaches statistically steady state at around 67000 steps, which corresponds to 5000s in physical time and $300T_e$. From this moment until the end of iteration $1800T_e$ the flow statistics are averaged. The entire averaging period is $1500T_e$, which is long enough that the flow can sufficiently settle down. The bulk velocity is used as the criterion for the statistical convergence and its evolution with time is shown in Figure 5.4.

For the flow over an inhomogeneous structure, the velocity may be decomposed as follows:

$$u_i = \langle \bar{u}_i \rangle + \tilde{u}_i + u_i', \quad (5.5)$$

where the $\langle \bar{u}_i \rangle$ is the double average over time and space, \tilde{u}_i is the dispersive part of the velocity, and u_i' is the turbulent fluctuation. In terms of the flows over smooth surface, for example, turbulent channel flow, the flow can be seen as homogeneous in space. When it reaches statistically steady state, the dispersive velocity can be averaged out, suggesting the spatial mean can be essentially equal to time mean. However, it is not the case for flows over inhomogeneous surface, with which the dispersive velocity cannot be smoothed out. The physical meaning of the dispersive velocity can be understood

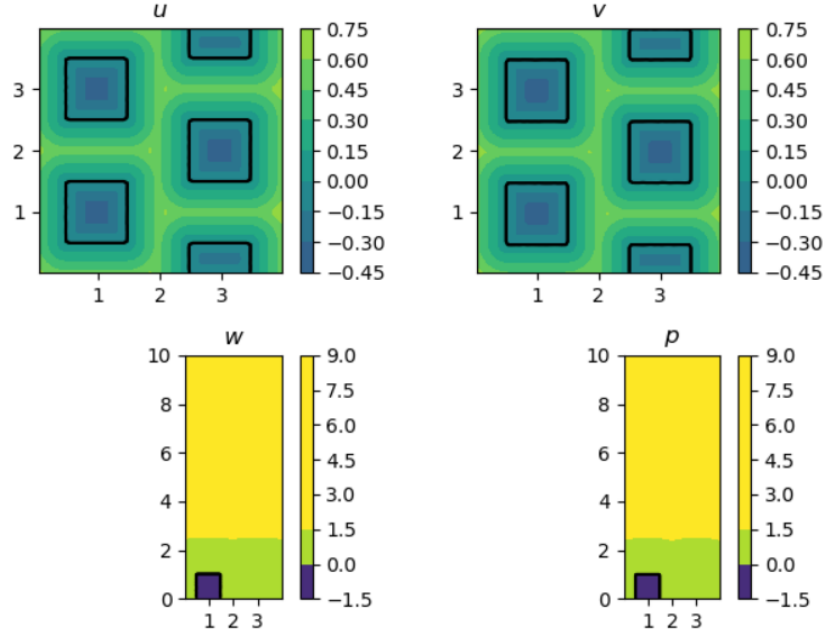


Figure 5.3: 2D slices of the generated SDF for u, v, w , and p location. The SDF of u and v are sampled at 10th grid in z direction, and the SDF of w and p are sampled at 10th grid in y direction. The black lines are the locations that the value of signed-distance is zero, represent the shape of the cube arrays.

as the deviation of the local time mean velocity of each cell to the spatially average time mean velocity due to the effect of the inhomogeneous structures.

According to Coceal et al., (2006), if the averaging time is not long enough, there could be a remaining low frequency streamwise recirculation right above the canopy. The slow evolving structures are commonly observed when fluids flow over rough surfaces. In this case, the remaining recirculation would significantly affect the dispersive part of the velocity and Reynolds stress. When the averaging period is long enough, these large recirculation flows move around and are smoothed out in the long time of sampling period, such that dispersive compositions cease to be significant. Coceal et al., (2006) indicates that for flow over cube arrays, when the averaging period is longer than $400T_e$, the dispersive Reynolds stress could become negligible compared with that within the cube canopy layer, and the slowly evolving recirculation structures no more exists.

The mean flow data are sampled every 10 iterations after the flow becomes steady until the end of the simulation. The sample interval is always smaller than $0.08s$ in physical time. This corresponds to around $0.05T_e$. In the code, several line probes are placed at the P0, P1, P2, and P3 locations indicated in Figure 5.1. Along the four lines, velocity data are collected through interpolation and then compared with the LES results from Tomas et al., (2016) and the wind tunnel experiment by Castro et al., (2006), in which the flow is generated under an inflow condition without accounting thermal effects. In the experiment, the flow above the cube array canopy was measured with hot-wire anemometry (HWA) and Laser Doppler Anemometry (LDA) within the canopy. The vertical profiles at the probe locations are obtained in the measurement and also made use to make comparison by Tomas et al., (2016). Both LES and the measurement reported similar results with H. Cheng and Castro, (2002) by having friction Reynolds number $Re_\tau = 371$.

Figure 5.5 shows the time-averaged streamwise velocity along the line probes. It can be seen that the current validation results generally show good agreement with the LES as well as the wind tunnel experiments. However, similar with the LES by Tomas et al., (2016), the current implementation slightly overestimates the streamwise velocities at locations P0, P1, and P3. The validation's results match with LES and experiments data well within the canopy at the locations. At location P2, LES by Tomas et al., (2016) slightly underestimates the streamwise velocity above the canopy could be caused by the overestimated wake region in LES, whereas the present validate achieves closer results to the

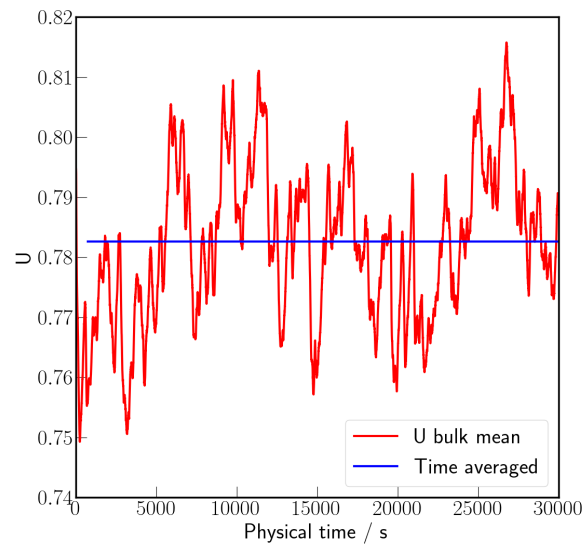


Figure 5.4: The change of the bulk streamwise velocity with physical time. The red line is the fluctuating bulk velocity at each time step, and the blue line is the time averaged velocity.

experiment. Additionally, within the canopy, the validation also shows better performance by having the profile closer to experiment data.

Figure 5.6 shows the resolved Reynolds stress at location P1 and P2. The resolved Reynolds stress $\overline{u'w'}$. It can be observed from the plots that general good agreement is achieved. At both locations, DALES code by Tomas et al., (2016) matches slightly better with the experiments, while the current validation tracks the shear layer better above the canopy. Neither LES could fully resolve the flow especially in the shear layer on the top of the cubes possibly due to the grid resolution. This same reason could reasonably also explain that within the canopy, part of the Reynolds stress is smoothed out because of the large grid spacing.

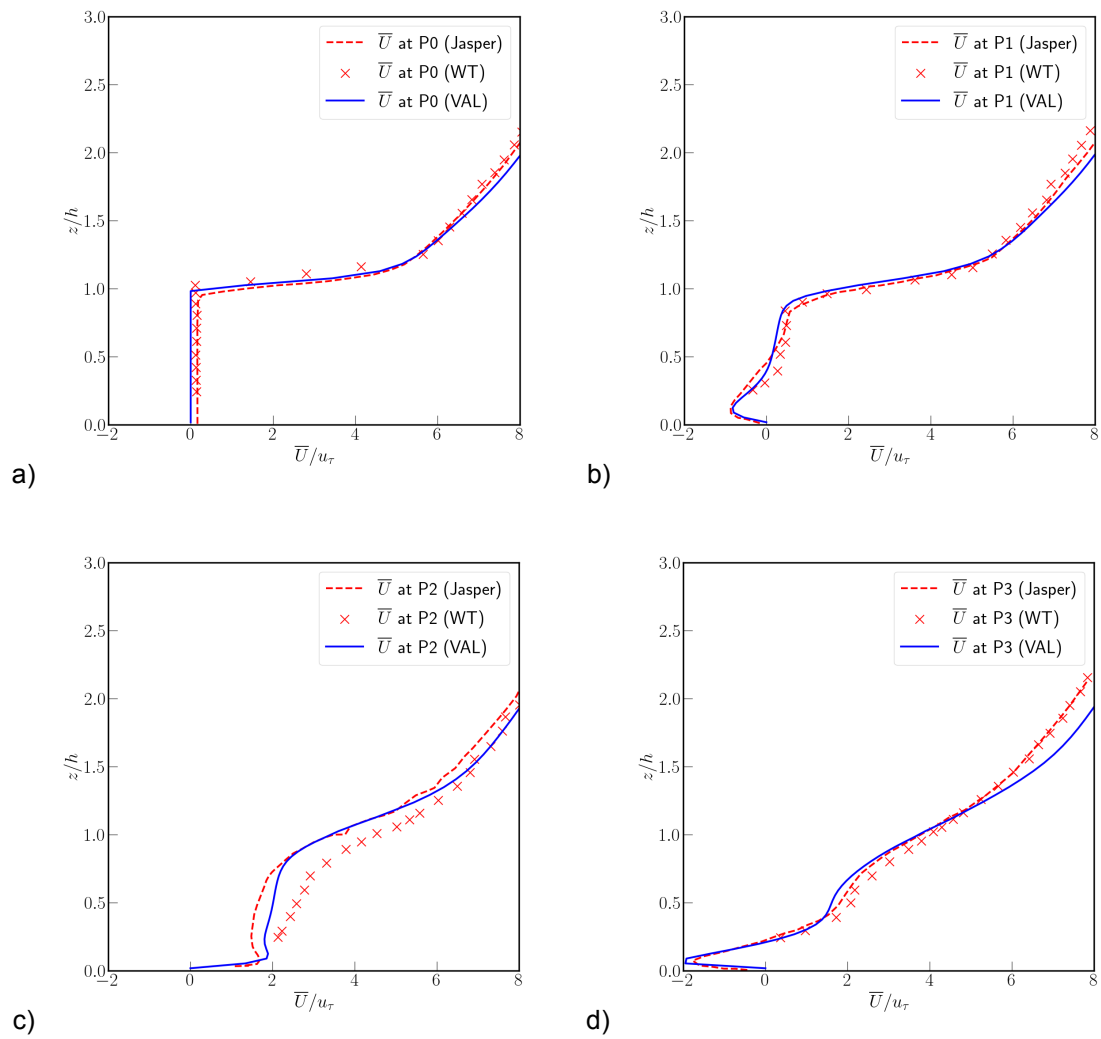


Figure 5.5: Time mean velocity along the four line probes. The red dashed lines are the LES data from Tomas et al., (2016), marked by (Jasper). Red cross are the data from wind tunnel measurement (WT) by Castro et al., (2006), and the red lines are the results from the current validation (VAL). The location of the line probes is shown in Figure 5.1.

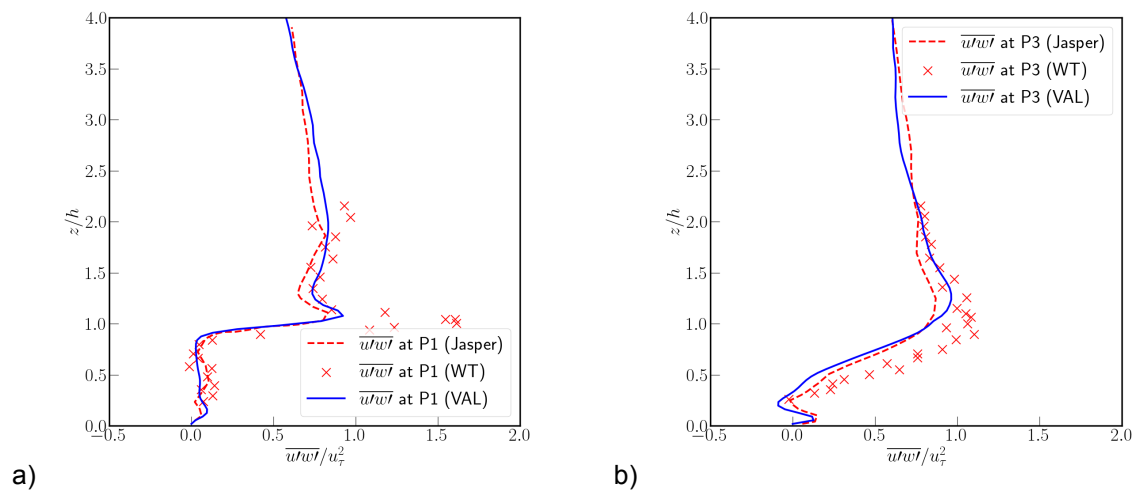


Figure 5.6: Time averaged Reynolds stress along the two line probes at location $P1$ and $P3$. The red lines are the LES data from Jasper, red cross are the data from wind tunnel measurement (WT), and the red lines are the results from the current validation (VAL).

6

Flow Over Delft Campus

Large Eddy Simulation (LES) model and Immersed Boundary Method (IBM) has been successfully implemented and validated in the previous two chapters. In the last step, LES and IBM are applied to a 3D model of an actual urban configuration. TU Delft campus is used as a case study. Such configuration has been studied by using actual size of the campus area with RANS (see Kenjereš and ter Kuile, (2013) and García-Sánchez et al., (2021)). However, they focus more on the effect of vegetation to the surface roughness and thus to the wind profile around buildings. The current study focuses on the effect of the inhomogeneous building topology on the formation of high speed area around a high-rise building and the wake region behind it. The high-rise building concerned is called EWI building (building for Faculty of Electrical Engineering, Mathematics and Computer Science), and it is believed to be the cause of a potentially dangerous high wind speed region near the building. To tackle such problem, it is worthwhile to study the wind around the EWI building under the context of flows over urban areas.

6.1. Introduction

This study focuses on TU Delft major campus area that is not far away from the EWI building. Thus the buildings of Faculty of Architecture, far north to the main campus, and buildings for Aerospace Engineering, far south to the main campus, are neglected for the simplicity of the model, because they are too far away to have significant impact on the wind around the EWI building and the main campus area. In addition, some newly built tall buildings east of the campus are neglected for the simplicity of the 3D model.

The building details are available by the 3D geo-information group from the Faculty of Architecture at TU Delft. High-resolution data regarding building topology and size are made open-source for multiple cities including all of the Netherlands, some cities in Germany, USA, and Singapore. According to García-Sánchez et al., (2021), the 3D models are classified into three main categories according to their level of details(LoD):

- LoD1: Buildings are represented with prismatic shapes. Flat rooftops are assumed to approximate the height of original buildings;
- LoD2: More detailed edges are added. Having simple roof shape (e.g. Sharp top of a church);
- LoD3: Semantics are utilised to denote different types of subjects or surfaces, such as grassland or water surface, in an urban environment.

LoD1 can be already satisfactory for the current research for the sake of simplicity. The object file is provided by 3D geo-information group. The solid structures representing the building geometries are generated using a so-called triangular decimation which is able to create a watertight geometry. It uses tetrahedrons to approximate object surface. Although the approximated flat building surfaces cannot be perfectly smooth by using tetrahedrons, they are good enough since the building size is huge compared to the small tetrahedrons size. Watertight 3D models are consequently generated such that

the leaking problem mentioned in section 3.5 can be avoided. According to García-Sánchez et al., (2021), the prevailing wind at TU Delft campus is south-west wind with 45° to the north.

6.2. Flow setup

The actual size of the simulated campus area is approximately $900m \times 700m \times 98m$. This is scaled down with a factor of $1 : 820$ to the size of $1.1m \times 0.85m \times 0.12$. Such campus region is then fit into a flow domain of dimension $L_x \times L_y \times L_z = 24H \times 22H \times 6H = 2.88m \times 2.64m \times 0.72m$, where the height of the EWI building in the scaled-down model $H = 0.12m$. The flow domain is set according to the Best Practice Guideline by Franke et al., (2007). The domain is large enough to contain the largest turbulent structures. The inflow boundary is put $6H$ west of the left boundary of the first building. The two sides are kept $6H$ away from their corresponding nearest building in the spanwise direction. The domain is $6H$ high to prevent the unwanted acceleration of the flow over the roofs. The most ideal choice for the vertical dimension is to keep it same with the corresponding wind tunnel size, with which a better overview of the growth of the roughness sublayer, inertial layer, even the urban boundary layer can be tracked. $6H$ is used here to reduce the computation cost. The distance between the building at the most east and the outflow boundary is around $10H$. Although it is suggested by Franke et al., (2007) that the distance should be at least $15H$, the pressure outlet boundary condition does not pose significant effect on the interested flow domain.

However, due to the limitation of computation power, it is impossible to resolve the full scale of the city, with which the Reynolds number would reach 3.3×10^7 given a calm wind speed of $5m/s$, based on the EWI height and actual air viscosity. Hence, it is necessary to scale the model down to a moderate Reynolds number that is achievable by LES. For the current phase of the code development, the LES needs to be wall-resolved, as wall function has not been incorporated in the solver.

An important consideration for the current research is the possible future duplication or the corresponding wind tunnel experiment using physical 3D models. It is hence reasonable to design the flow setup accordingly with the setup of a model for wind tunnel experiment that future researchers would like to do. Reference experiment resources, for example, the capability of wind tunnel test section, should therefore be taken into account.

An excellent reference could be the GVPM wind tunnel at Polimi (Polytechnic University of Milan) (see Lamberti et al., (2020)). It has a boundary layer test section of $13.84m$ wide, $3.84m$ high, and $35m$ long. The wind tunnel is specifically designed for wind engineering tests on civil structures scaled models. The maximum wind speed can reach $16m/s$. The $35m$ long, constant section test room enables the turbulence generators to simulate the atmospheric boundary layer, with the highest turbulence intensity around 35%.

As mentioned in the previous paragraph, the urban model is therefore scaled down to $H = 120mm$. With EWI height $H = 120mm$, the entire flow domain is $L_x \times L_y \times L_z = 24H \times 22H \times 6H = 2.88m \times 2.64m \times 0.72m$, which is able to fit in such wind tunnel with enough space to all walls, especially to the sides and the top. An incoming reference wind speed of $U_H = 2m/s$ can be prescribed at $H = 120mm$ and leads to a Reynolds number of

$$Re_H = HU_H/\nu = 0.12 * 2/(1.48 * 1E - 5) = 16216, \quad (6.1)$$

where $\nu = 1.48 \times 10^{-5}m/s^2$ using the actual air viscosity at 15° temperature.

Besides, the velocity $U_H = 2m/s$ is achievable in the wind tunnel. because with the log profile, even if the UBL stretches until the top of the wind tunnel, $U_{top} = 3.3m/s \ll U_{max} = 16m/s$. It has been intentionally avoided to use an U_H too in order to allow the flow to be resolved by the current LES. At the same time, an H too small is also intentionally avoided. The reason is that, if H is smaller, for example, $H = 60mm$, the average building height would be around $20mm$, and some lower building models could be even smaller. It could be possible that such small physical models are hard to fabricate and measure.

6.2.1. Boundary Condition

The boundary conditions should also consider the achievability in the wind tunnel test. The wind tunnel for urban boundary layer test has a long development distance of around 10 times of the atmospheric boundary layer (see Plate, (1999)). Attention is paid mainly to the wind velocity profile and turbulence intensity under neutral conditions. Usually, an uniform airflow from the wind tunnel entrance can be proscribed. The bulk flow is slowed down at the developing stage, then a down-scaled atmospheric boundary layer (ABL) like profile can thus be formed. Although the wind speed in such profile stays uniform in the spanwise direction and only varies with the height, turbulence intensities can be prescribed to approximate the turbulence effect.

In general, logarithmic functions Maruyama and Ishizaki, (1988) and the empirical power function J. Liu et al., (2018) can be used to describe such velocity profile as a function of the height. According to Bendjebbas et al., (2016), the logarithmic law is reported to be more suitable when having a domain higher than 300m. One of the inflow velocity profile logarithmic law can be written as:

$$u(z) = \frac{u_\tau}{\kappa} \ln\left(\frac{z + z_0}{z_0}\right). \quad (6.2)$$

Another expression for the logarithmic law can be commonly seen in the literature:

$$u(z) = \frac{u_\tau}{\kappa} \ln\left(\frac{z - d}{z_0}\right), \quad (6.3)$$

same as the one mentioned in the previous chapter. The two formula are explained in the following paragraphs.

The difference could be related with the stratification of the urban boundary layer (UBL). The UBL generally consists of two part, the inner layer and outerlayer. The inner layer can be partitioned into the inertial sublayer (ISL) and the roughness sublayer (RSL). Within the ISL the flow can be seen as homogeneous, the vertical variation of the shear stress can be neglected and the wind direction could be assumed constant with height. The above equation 6.3 can describe the wind speed. In equation 6.3, the friction velocity u^* represents the effect of wind stress on the ground. z_0 is the roughness length, which means the distance where the wind speed theoretically becomes zero under neutral conditions in the absence of the obstacles that slow down the wind down. It is observed to increase with the increase of the roughness height. d is the zero plane displacement height, it could be regarded as the level of surface at which the mean drag acts. Below the ISL until the ground is the RSL, in which the urban canopy is at its lowest part. RSL is believed to be 2 to 5 times of the roughness height (see H. Cheng and Castro, (2002)). Within the RSL, the logarithmic law does not hold due to the inhomogeneity of the flow.

However, the ISL is usually found "squeezed" between the outerlayer and the RSL, so there is no clearly defined logarithmic profile. From what is understood by the author, equation 6.2 could be a compromise between considering collectively both the lengthscale of the ISL and the outerlayer, such that at every location inflow logarithmic inflow profile can be defined. Although in the outerlayer the mean velocity may greatly deviate from the logarithmic profile Maruyama and Ishizaki, (1988).

In the current research, formula 6.2 is used as a simple inflow velocity condition with 5% random noise in all directions. Table 6.1 shows the common values of roughness length that can be used for different surface configurations. Considering the low height and coarsely distributed buildings around TU Delft campus, $z_0 = 0.5m$ is assumed under the context of the actual building height. Consequently, in the simulation model, it could be a good practice to scale the z_0 down according to the scaling factor same with the campus model. $z_0 = 0.006087m$ is the scaled down roughness length, and $u_\tau = 0.155m/s$ is friction velocity.

To summarize the boundary conditions, at the inflow, the flow comes perpendicularly into the domain with only variations with z coordinate. Zero velocity is imposed at inflow in both spanwise and vertical

Terrain	$z_0(m)$
Tall buildings and complexes	≥ 2
Tall buildings with high-density	0.8 – 2
Medium height buildings with moderate-density, town center	0.7 – 1.5
Low height buildings with low-density, suburb	0.3 – 0.8

Table 6.1: Roughness length for different surface configuration (see Zhao et al., (2022)).

direction. 5% Random noise is added for all directions. Pressure outlet outflow condition is used in x direction, with zero velocity gradient in all directions and a prescribed reference pressure. In the spanwise direction, both sides are free-slip, and no flow can penetrate the boundaries. On the ground, the ground and the building surfaces are no-slip and not penetratable. The top surface is the same as the side boundaries, represented by zero velocity in along the normal direction and zero velocity gradient in parallel directions.

6.2.2. Grid Resolution

The simulations use the same size of the flow domain as the proposed model in the previous paragraph for the wind tunnel measurement setup, to avoid the misleading part of rescaling the wind velocity, EWI height, and air viscosity according to Reynolds number similarity. In the simulation, the air viscosity uses the actual kinematic air viscosity under $15^\circ C$, $\nu = 1.48 \times 10^{-5} m/s^2$.

It is too costly to fully resolve the flow down to the smallest scale of eddies at the structure boundary to get wall-resolved results. Hence, an approach similar with grid convergence analysis is adopted. Three types of grids are used. The difference of their results are compared to gain insights of the flow. The dimensions of the three grids are $N_x \times N_y \times N_z = 480 \times 440 \times 120$, $N_x \times N_y \times N_z = 720 \times 660 \times 180$, and $N_x \times N_y \times N_z = 960 \times 880 \times 240$, respectively. For each grid along z direction, one-third of the number of the grid is uniformly distributed within the canopy. The grids are uniform in x and y direction, and also uniform within the canopy height H in z direction. Above H , grid generation function same with equation 6.4 is applied again:

$$zf_k = 1 \left[1 + \frac{\tanh(\frac{k}{N_z} - 1)gr}{\tanh(gr)} \right], \quad (6.4)$$

with a growth rate $gr = 1.25$, such that the cell volume growth ratio is no greater than 1.04.

6.3. Results

6.3.1. Signed-Distance Field

The workflow is similar to the previous chapter. Firstly the SDFs are generated with "STL2SDF" and then checked using isosurfaces and 2D slices. In "STL2SDF", the number of sampling point is 4000000 such that it is not only sufficiently large to be able to accurately represent the boundary, but also not too large that exceeds the memory limit of Delftblue server, which is the cluster used for the iteration for the current project. Three isosurfaces are generated each case for the SDF of u, v , and w due to the staggered arrangement. Figure 6.1 shows an example of the SDFs of velocity u locations, denoted as sdf_u .

It is worth mentioning that, the grid resolution significantly affects the isosurfaces. As shown in Figure 6.1, when the grid resolution increases, the edges of the building become clearer. As in picture a), the original sharp edges of the squared roofs or the devices installed on the rooftop that are supposed to be represented by the raised prism are smoothed out. Also, some originally thin roofs are interpreted as sharp edges. The rendering error when plotting isosurfaces in MATLAB also contribute to such distortion. As the grid resolution increases, the more complex shapes are better represented, and in picture d) the entire campus is clearly interpreted by tetrahedrons.

Similar to the SDF of the cube arrays, when rendering the isosurface, MATLAB can give false curvature or peaks where the SDF must be continuous. To precisely examine the SDF one would like to compute

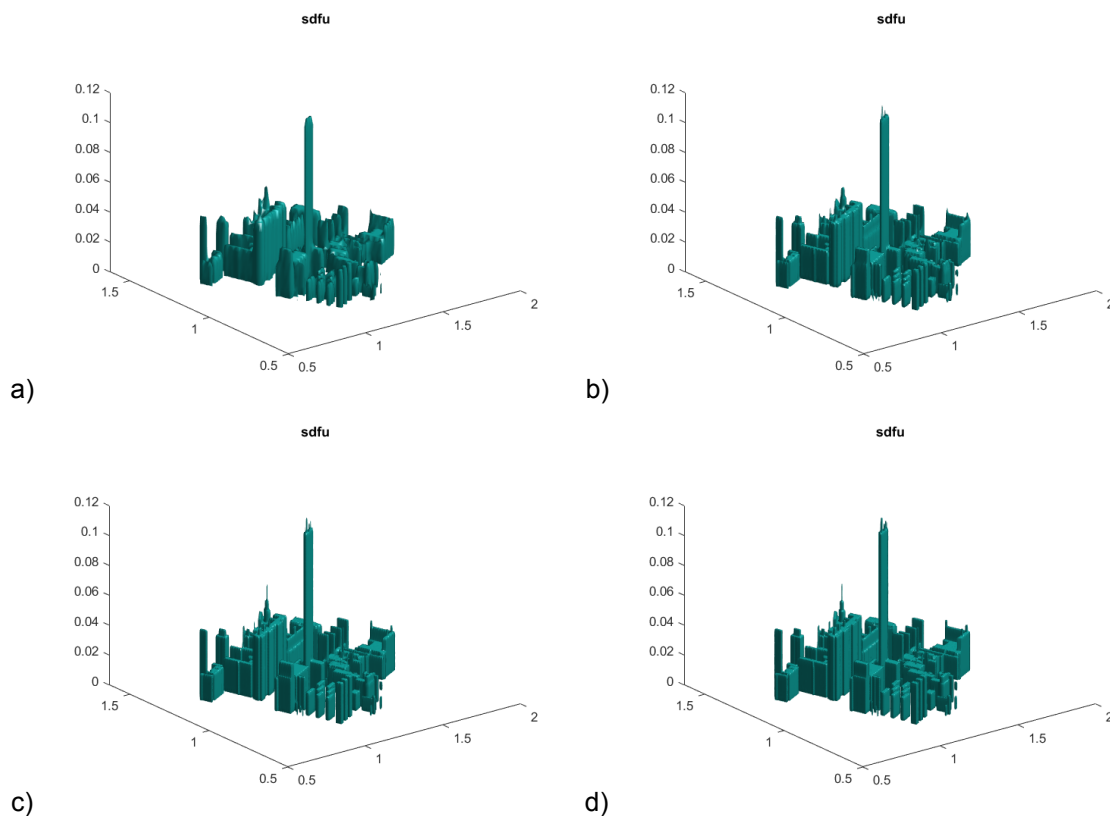


Figure 6.1: Four iso-surfaces of the SDF of u for the scaled-down campus model generated with MATLAB. Grid resolution are different with a) $240 \times 220 \times 60$, b) $480 \times 440 \times 120$, c) $720 \times 660 \times 180$, and d) $960 \times 880 \times 240$.

the gradient of SDF. A convenient alternative way is to check the 2D slices of the SDFs given that the isosurface overall appear to have no problem. The 2D slices of the SDF of u with the finest grid case is shown in Figure 6.2. In the current model, EWI building is the only high-rise building. It can be observed that With the increase of the vertical grid index, fewer buildings remain in the 2D slices, indicating that the SDFs are reasonably represented.

To further gain insight into the turbulent characteristics. 14 line probes in total are inserted in the urban area. 6 are uniformly distributed in the urban area with the spacing $2H$ and $3H$ in x and y direction, respectively. The rest 8 probes are placed around the EWI building, which is of major interest. Among these 4 are in the possible high-speed region in the path north to the EWI building, and the other 4 are in the possible wake region east to the EWI building. Their numbering and position are shown in Figure 6.3. The line probes are vertically inserted in the domain and sample the cell-centered values of probed quantities for simplicity.

6.3.2. Grid Convergence

LES, in some sense is under-resolved by nature – The unresolved scales smaller than the filter length are intentionally filtered out and modeled. As the grid resolution increases, the spectrum resolved scales is wider, since the smaller scales are explicitly resolved, and the range of unresolved scales are getting smaller. In this sense, the meaning of grid-convergence of LES is object of debate. However, several approaches could help to define the feasibility of the grid. It is suggested by Pope, (2001) that the ratio of unresolved turbulent kinetic energy (TKE) to the total TKE should be lower than 20% such that the accuracy of local LES can be assured. A strict approach is to explicitly show the energy spectrum and make sure the cutoff length scale is in the inertial range, which guarantees that the eddies containing most energy are resolved (see Toosi and Larsson, (2018)). A convenient and practical approach suggested by Council et al., (2012) indicates that, the grid convergence can be evaluated by “quantities of interest” (QoIs), which are the output parameters that researchers are interested in. This

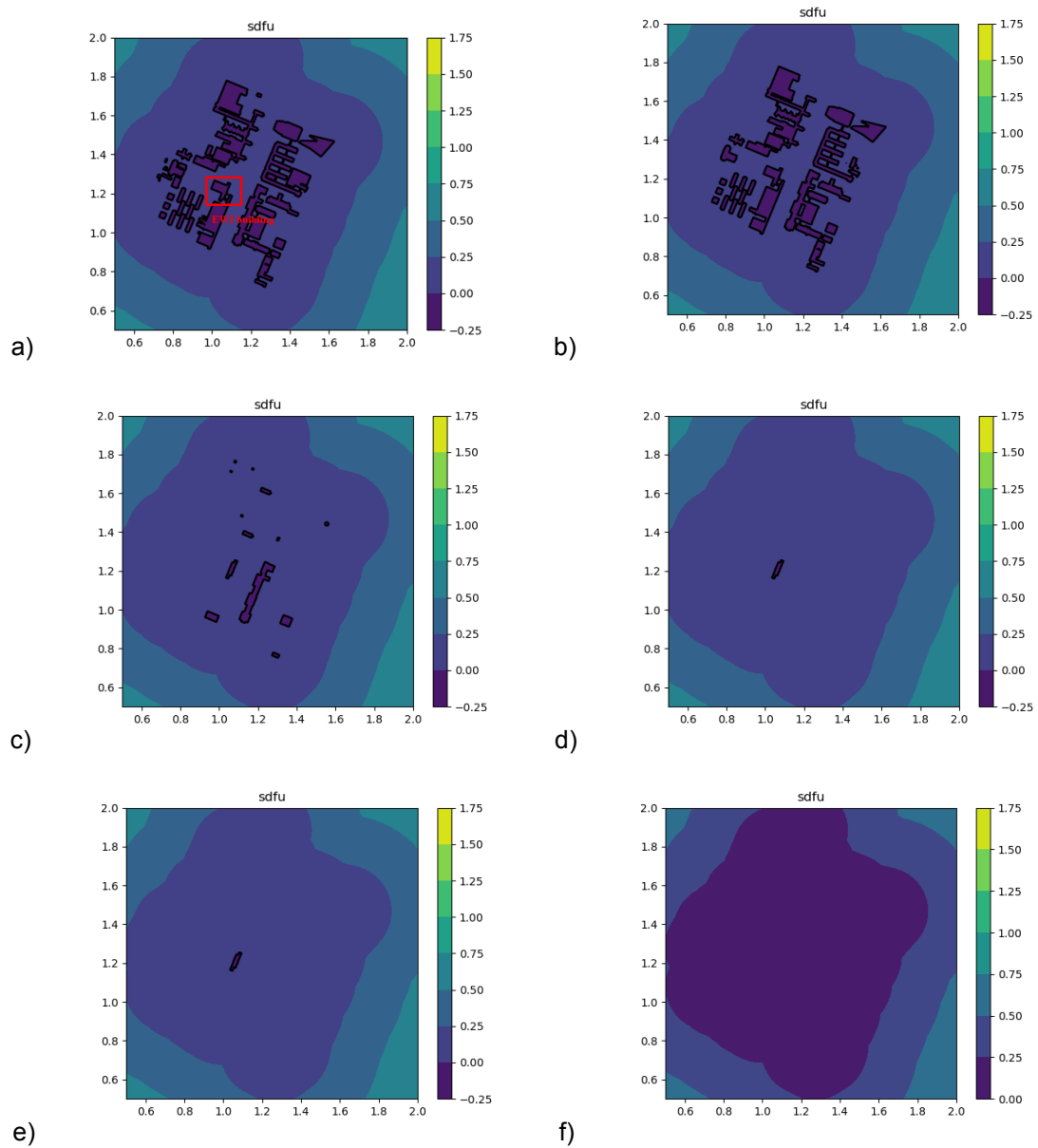


Figure 6.2: 2D slices of the SDF of u with different height using the $960 \times 880 \times 240$ grid. The black lines denote the locations where the signed distance values are equal to 0, representing the boundary of buildings. The EWI building is marked in the red box in picture a). The slices corresponds to the height of the a) 5th, b) 10th, c) 20th, d) 40th, e) 60th, f) 80th grid in z direction.



Figure 6.3: Top view of the model used for the current simulation, only the urban area is shown. The colored points show the location of the vertical line probes. The green points are the points uniformly distributed, red ones are at the possible high-speed region, and the blue ones are at the possible wake region. The EWI building is marked with the red box.

approach is adopted for the current research, and the concerned QoIs include total IBM forcing, mean velocity, and corrected Reynolds stress. The corrected quantities are the summation of the resolved ones and unresolved ones. The resolved or unresolved quantities alone cannot be used as the criteria since they converge only to DNS.

6.3.3. IBM Forces

All of the three cases are stopped at 159390, 134593, and 113101 steps, and have reached physical time of around $350s$, $150s$, and $100s$. Again, the CFL number never exceeds 0.95; the simulations are stopped until the total forces have converged for a sufficiently long time. The eddy turnover time is $T_e = \frac{H}{u_\tau} = \frac{0.12}{0.155} = 0.775s$, and the statistics are averaged after $5s$ in physical time until the end of the iterations. In all three cases the averaging periods are longer than $103T_e$. For comparison reason, only around the first $100s$ after convergence are shown. The total IBM force is used as the statistical convergence criteria for the simulations. The force is obtained by directly summing up the IBM force that the structure imposes on the fluid, and it, by definition, includes both pressure-induced drag and viscous-induced drag forces.

Figure 6.4 shows the evolution of total IBM forces with physical time. IBM forces rapidly converge to certain values only after a short period of initialization. Their converged values are summarized in Table 6.2. It may be observed with the finer grid, the IBM forces have shown signs of converging. However, the values to which the forces converge do not vary significantly with different meshes. Even for the most coarse mesh, which is apparently not enough for resolving the flow, the total forces are close to the results of the finest mesh. A possible reason is that the grid spacing at the boundary is not fine

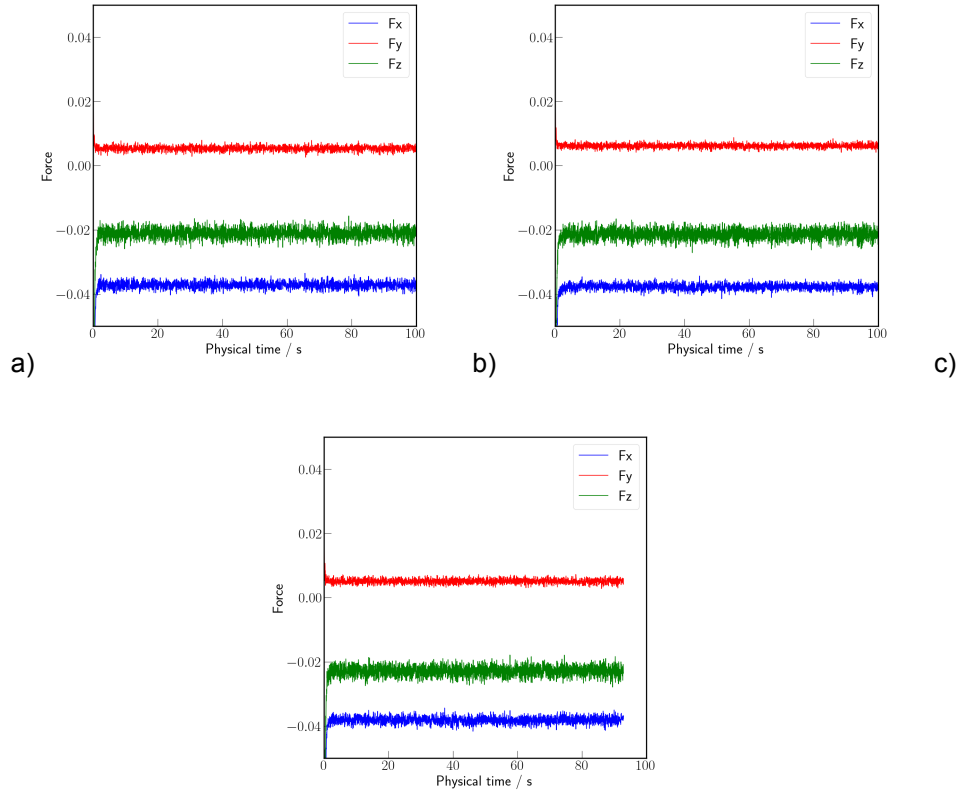


Figure 6.4: Total IBM forces exerted by the structure boundary on the fluid using different grid resolution, with a) $480 \times 440 \times 120$, b) $720 \times 660 \times 180$, and c) $960 \times 880 \times 240$ mesh.

Grid resolution	F_x	F_y	F_z
$480 \times 440 \times 120(40)$	-0.03729	0.00536	-0.02118
$720 \times 660 \times 180(60)$	-0.03801	0.00618	-0.02163
$960 \times 880 \times 240(80)$	-0.03860	0.00513	-0.02331

Table 6.2: Total IBM forces acting on the fluid. The number in the symbol () is the number of grid within canopy in z direction.

enough, for example, the 1st grid point is not in the range of $y^+ \leq 1$, which is generally believed to be one of the wall resolution requirements. In this case, on the top of the canopy, the first cell center near the boundary falls into the buffer layer ($y^+ \geq 5$) and cause the boundary layer imprecisely tracked. At the same time, it is difficult to determine whether the flow truly achieves grid convergence using total IBM force criteria solely, more data is needed.

6.3.4. Mean Velocity

Mean velocity data are collected along the line probes, the time-averaged results are separately shown in Figure 6.5, Figure 6.6, and Figure 6.7 depending on their located region. In the plots, spacing along x axis is made to allow multiple plots to fit in the same figure, with their corresponding tick node value representing the zero value "origin". For example, in Figure 6.5 - 6.7. The spacing of the plots for different locations is 4.

From Figure 6.5 to Figure 6.7, signs of convergence can be also found using the three types of grid. Above the canopy, the flow follows logarithmic law that is similar with the inflow condition, and at height $h \geq 0.15m$, which is around 1.25 times the height of the scaled-down EWI building, the mean flow profile is no more affected by the urban structure. Within the canopy layer, velocity profile at location 2 and 6 are found to have zero value, because the line probe there is inserted into the building structure. High speed can be observed at the probe location at 7 - 10. This is because the moderate-high building at

the two sides blocks the wind flow, forcing the air to flow through this narrow channel. It can be seen that when using coarse grid, the plots deviate from the logarithmic profile. This may be a dispersive error caused by insufficient grid resolution. In Figure 6.7, back-flow can be suggested within the canopy. At around $H = 0.12m$, the air velocity reduces to a low level due to the blocking effect of the EWI building. At the back side of the building, a wake region can be suggested at location 11 – 14, characterized by the close-to-zero wind speeds in the middle, and slow sub-zero speeds in the lower parts. At probes 13 and 14, relatively higher speed can be found again at a height close to the ground. One possible reason is that due to the presence of other moderate-high buildings and the ground, air has to flow away at this height due to conservation of mass. Figure ?? shows a figure demonstrating the velocity magnitude at ground level.

6.3.5. Corrected Reynolds Stress

The Results of the corrected Reynolds stress $\overline{u'u'}$, $\overline{v'v'}$, $\overline{w'w'}$ are shown in Figure 6.8 to 6.16, and they are classified depending on the probe locations. The resolved and unresolved Reynolds stress are obtained using the same formula as in the Chapter 4. The plots are shifted right in a similar way as for the mean velocity.

Figure 6.8 to 6.10 are the corrected Reynolds stress at the line probe locations that are uniformly distributed. It can be seen that most of the turbulent characteristics exit within the canopy height $H = 120mm$. Above the canopy, Reynolds stress cease to be significant at $175mm$. Two representative locations are 2 and 6, at these two positions, the probe lines are both inserted in the buildings, and the tallest buildings are only around one-third of the height of the EWI building. When the height is lower than the top of the local building, all Reynolds stress values are zero, while at the top of the building, a shear layer can be clearly observed. The Reynolds stress profiles that extend to around 2 – 3 local building height could result from the local roughness layer formed by the interaction between flow and the surrounding structures.

As for probe location 1, the regularly shaped and located houses close to it have even lower height. This appears insufficient to explain that the Reynolds stress extends to a height of $75mm$. However, at further upstream and direct downstream of location 1 there are buildings with moderate height (around one-third of EWI building). The further upstream buildings are the three cube-like complexes at the west of campus area, and at the direct downstream is the long-thick building. It is reasonable to speculate that the Reynolds stress profile here could be either originated from the turbulence effect from the cubic complexes or the effect from direct downstream building. Location 3 is at direct downstream of a group of buildings with medium heights, which gives it a Reynolds stress profile similar with at locations 2 and 6, but because it is not directly inserted into the building structure, it has a complete profile within canopy.

Location 4 is directly upstream of some low-rise buildings. Therefore, it is possible that the relatively thin roughness layer comes from the other low-rise buildings more upstream on the two sides. Location 5 seems to be special because it is unluckily located at the high-speed fluid area next to one of the medium-height towers of the 3ME building (Faculty of Mechanical, Maritime and Materials Engineering). It thus shows a similar profile with the high-speed area around EWI building below. Because 3ME building is relatively low in its height, the roughness layer at location 5 is also shorter than that of EWI building.

Figure 6.11 to 6.13 are the corrected Reynolds stress profiles in the high-speed area. With the refining of the grid, the results appear to converge to certain values. In this region, the Reynolds shear stress are small because there is no significant shear layer in high speed region. The low values could be originated from the turbulence effect of the buildings near the locations. The relatively higher Reynolds stress near the ground could be from the influence of the flow around the corners. Figure 6.15 to 6.16 show the corrected Reynolds stress in the wake region behind the EWI building. A large shear layer can be observed right above the canopy, and extends until $175mm$ high, which is around $1.5H$. This could be caused by the flow over the buildings.

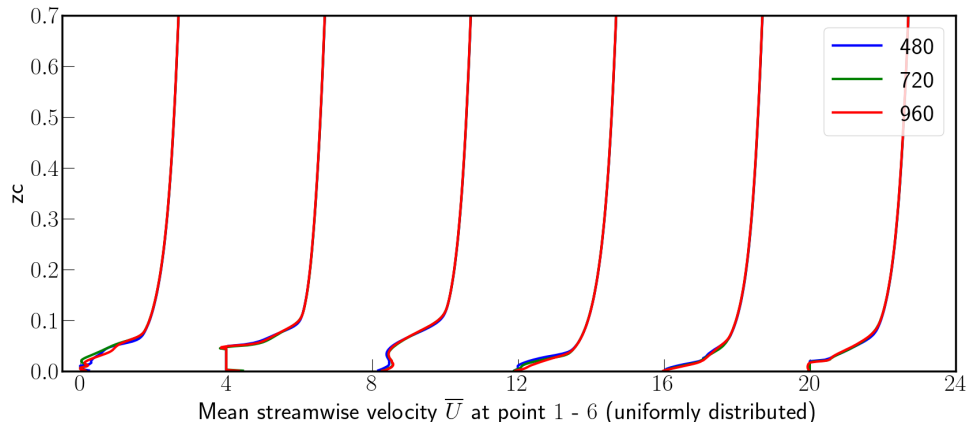


Figure 6.5: Streamwise time averaged velocity at lineprobes 1 – 6 (uniformly distributed).

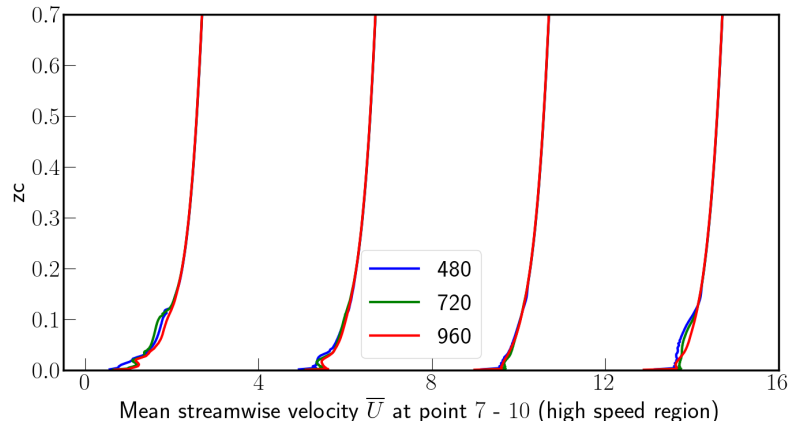


Figure 6.6: Streamwise time averaged velocity at lineprobes 7 – 10 (high speed region).

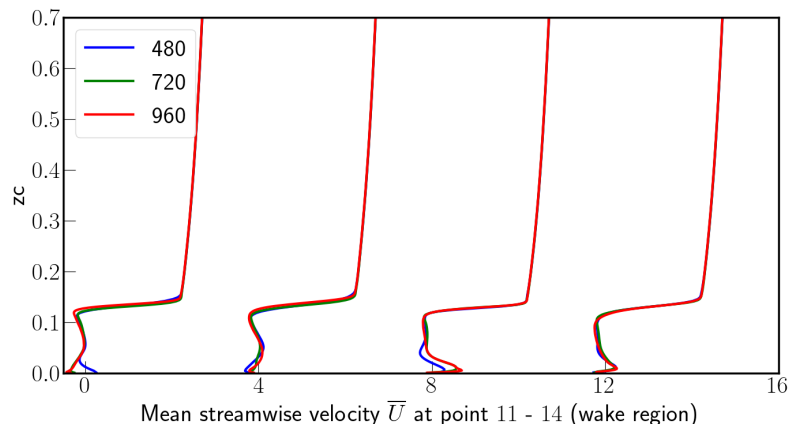


Figure 6.7: Streamwise time averaged velocity at lineprobes 10 – 14 (wake region).

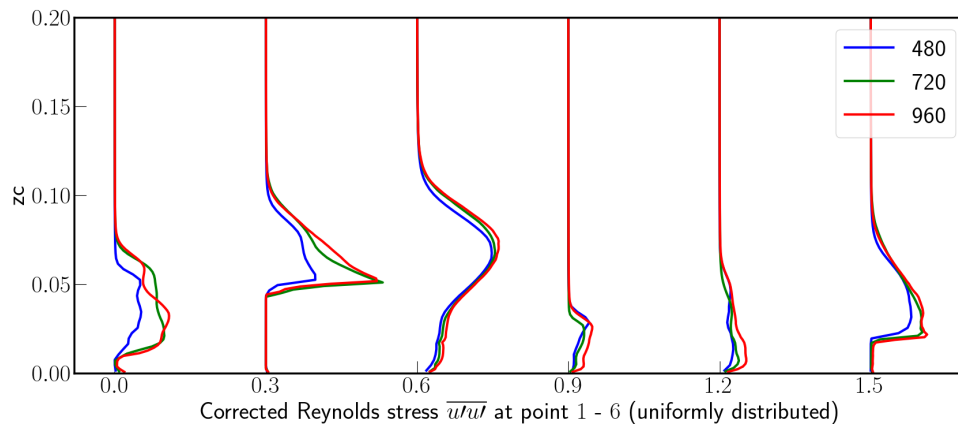


Figure 6.8: Mean (time) Reynolds stress $\overline{u'w'}$ at probe 1 - 6 (uniformly distributed).

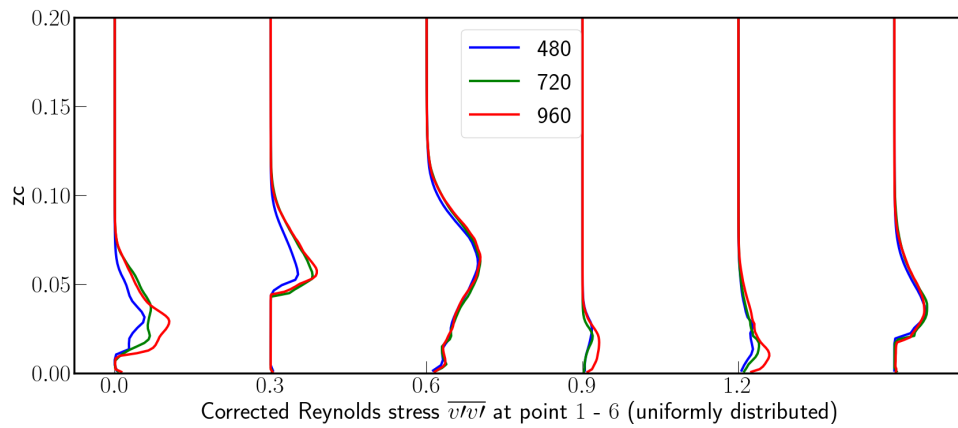


Figure 6.9: Mean (time) Reynolds stress $\overline{v'v'}$ at probe 1 - 6 (uniformly distributed).

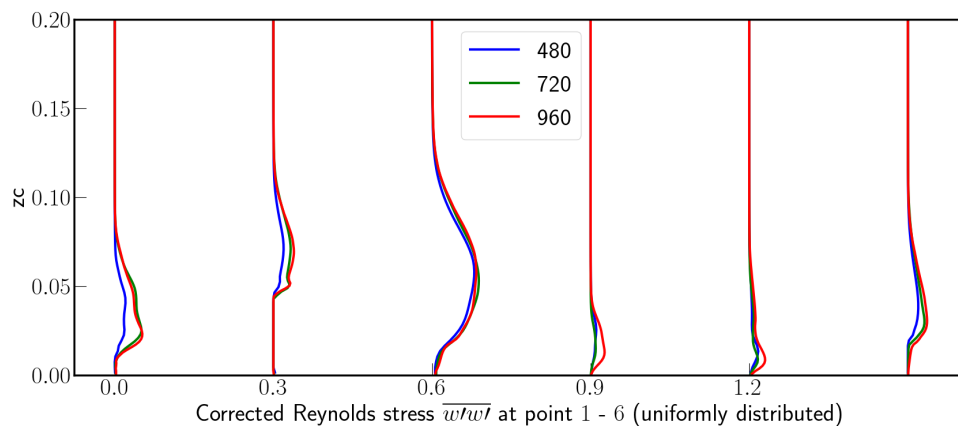


Figure 6.10: Mean (time) Reynolds stress $\overline{w'w'}$ at probe 1 - 6 (uniformly distributed).

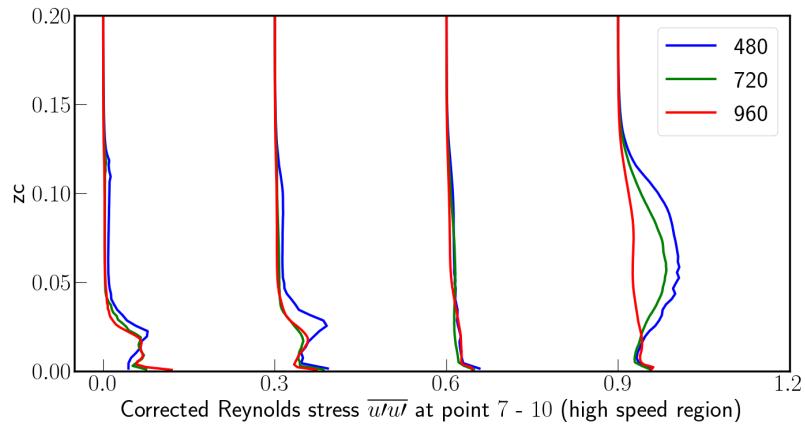


Figure 6.11: Mean (time) Reynolds stress $\overline{u'w'}$ at probe 7 - 10 (high speed region).

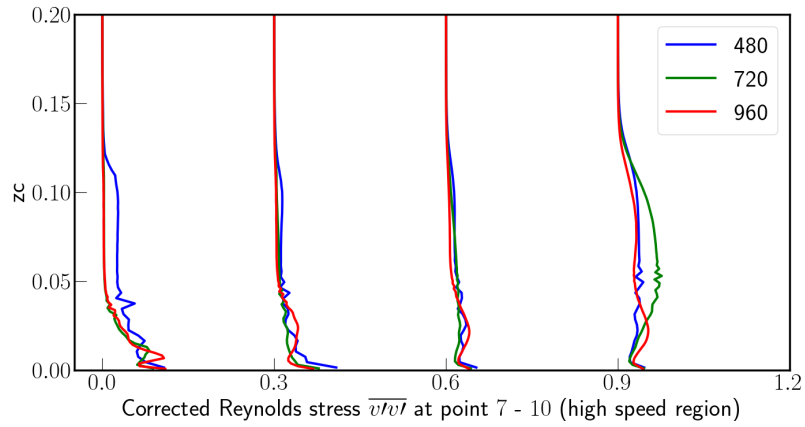


Figure 6.12: Mean (time) Reynolds stress $\overline{v'v'}$ at probe 7 - 10 (high speed region).

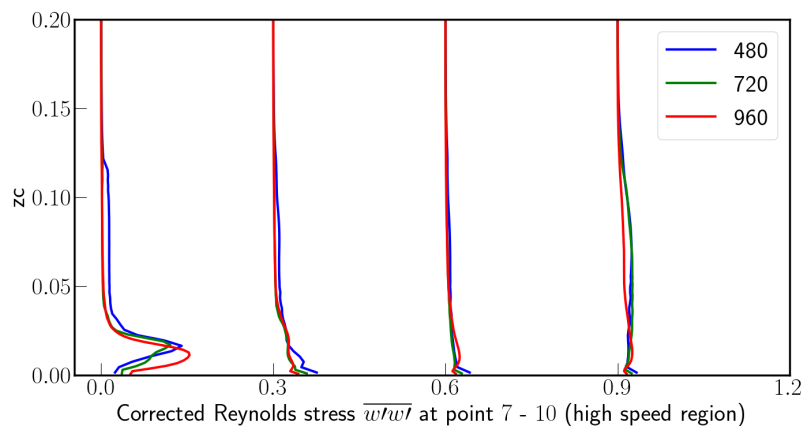


Figure 6.13: Mean (time) Reynolds stress $\overline{w'w'}$ at probe 7 - 10 (high speed region).

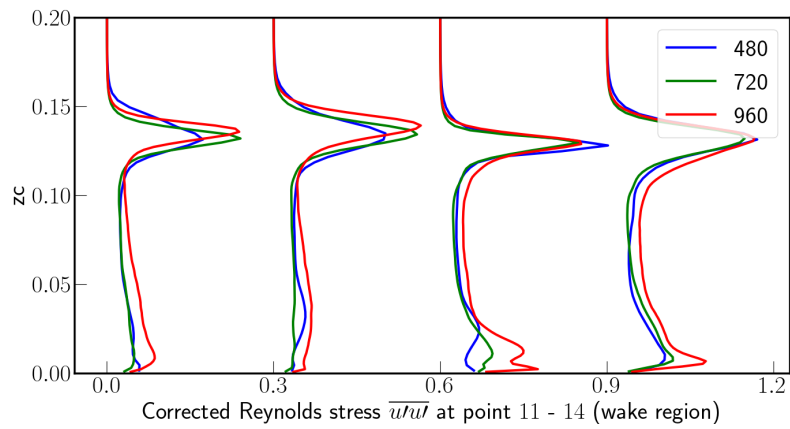


Figure 6.14: Mean (time) Reynolds stress $\overline{u'u'}$ at probe 10 - 14 (wake region).

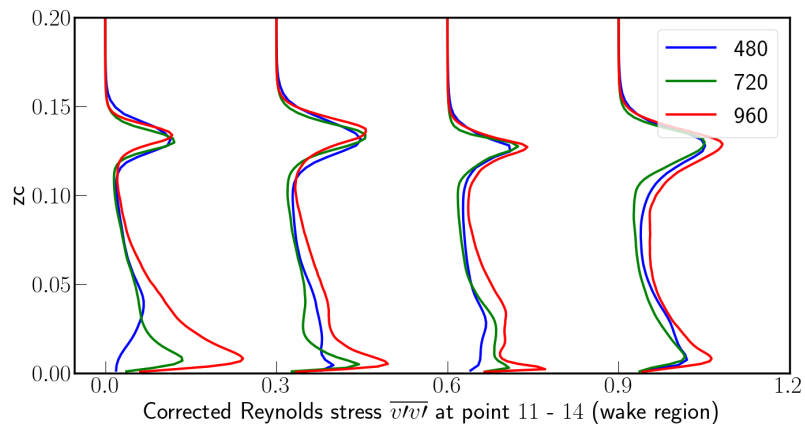


Figure 6.15: Mean (time) Reynolds stress $\overline{v'v'}$ at probe 10 - 14 (wake region).

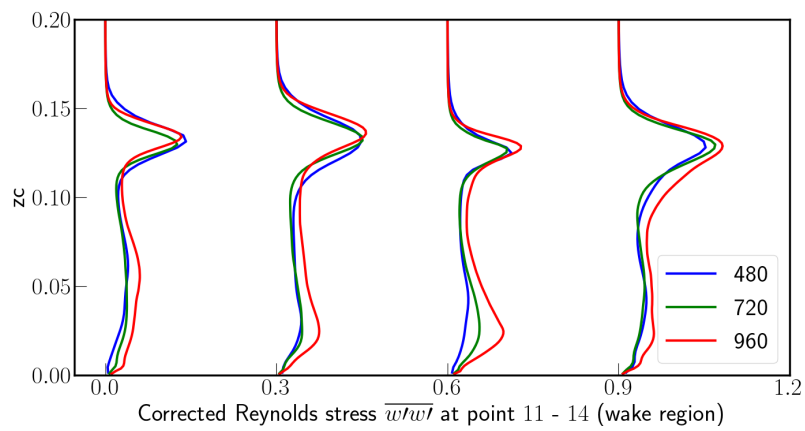


Figure 6.16: Mean (time) Reynolds stress $\overline{w'w'}$ at probe 10 - 14 (wake region).

7

Conclusion and Future Work

Urban flow is a vital aspect of urban microclimate. Strong wind at pedestrian level in urban areas affect people's perceptive comfort. This thesis focused on the urban configurations by using LES through implementing the Vreman eddy viscosity model in CaNS. The LES implementation had achieved excellent agreement according to the turbulent channel flow validation. The code was subsequently inserted with a stair-step IBM. SDFs were generated with the code STL2SDF and used as input data for the IBM. This approach was validated with flow over cubic arrays having $Re_\tau = 371$. Compared with experiment and previous LES data, the results for mean velocity and resolved Reynolds stress showed excellent agreement, and proved the approach to be valid.

Such method was then applied to a scaled-down 3D model of an actual urban area by taking the campus area of TU Delft as a case study. Grid convergence was analyzed. The results verified the existence of a high speed area near the EWI building at pedestrian level, and showed the wake region at the leeward side of the building as well as a shear layer on the building top.

Due to time limit of the current work, some simplified factors can be improved in the future work:

- First, the current code is facing issues with the decomposition of interpolation points into different computation blocks when using the interpolation approach by Yang and Balaras, (2006), as mentioned in chapter 3. With this error fixed, the boundary can be more accurately represented and more accurate forcing can be achieved;
- Second, the current inflow boundary condition for campus areas concerns a velocity profile that only varies with vertical coordinate. The turbulent effect is approximated by adding a random noise. However, this omits the inherent correlation of velocity and pressure, as well as the characteristic coherent structures of turbulence. An alternative could be using a recycling inflow boundary condition proposed by Lund et al., (1998), which preserves the turbulence structures that are difficult to reconstruct;
- Third, this research does not apply any wall function and tries to conduct wall-resolved simulations for urban models. However, this requires having large number of grid cells. According to Solinas et al., (2008), within the boundary layer, the number of grid point needed in the outer layer is proportional to $Re^{0.6}$ and for the inner layer is $Re^{2.4}$. It is believed that near the wall an LES should be able to resolve down to the inertial range, while this could be hard to examine. In this sense, replacing the inner layer with wall functions would be highly advantageous.

Bibliography

- Ahmad, K., Khare, M., & Chaudhry, K. ((2005)). Wind tunnel simulation studies on dispersion at urban street canyons and intersections—a review. *Journal of Wind Engineering and Industrial Aerodynamics*, 93(9), 697–717.
- Allegrini, J., & Lopez, B. ((2016)). The influence of angular configuration of two buildings on the local wind climate. *Journal of Wind Engineering and Industrial Aerodynamics*, 156, 50–61.
- Barulli, M. ((2022)). *Pollutant dynamics in urban canyons: Wind-tunnel experiments and numerical simulations* [Doctoral dissertation, Politecnico di Torino].
- Bendjebbas, H., Abdellah-EIHadj, A., & Abbas, M. ((2016)). Full-scale, wind tunnel and cfd analysis methods of wind loads on heliostats: A review. *Renewable and Sustainable Energy Reviews*, 54, 452–472.
- Beranek, W. v., & Van Koten, H. ((1979)). Beperken van windhinder om gebouwen, deel 1. deventer: Stichting bouwresearch no. 65.
- Blocken, B. ((2015)). Computational fluid dynamics for urban physics: Importance, scales, possibilities, limitations and ten tips and tricks towards accurate and reliable simulations. *Building and Environment*, 91, 219–245.
- Blocken, B. ((2018)). Les over rans in building simulation for outdoor and indoor applications: A foregone conclusion? *Building Simulation*, 11(5), 821–870.
- Blocken, B., & Carmeliet, J. ((2008)). Pedestrian wind conditions at outdoor platforms in a high-rise apartment building: Generic sub-configuration validation, wind comfort assessment and uncertainty issues. *Wind and structures*, 11(1), 51–70.
- Blocken, B., & Carmeliet, J. ((2004)). Pedestrian wind environment around buildings: Literature review and practical examples. *Journal of Thermal Envelope and Building Science*, 28(2), 107–159.
- Blocken, B., Janssen, W., & van Hooff, T. ((2012)). Cfd simulation for pedestrian wind comfort and wind safety in urban areas: General decision framework and case study for the eindhoven university campus. *Environmental Modelling & Software*, 30, 15–34.
- Bruse, M., & Fleer, H. ((1998)). Simulating surface–plant–air interactions inside urban environments with a three dimensional numerical model. *Environmental modelling & software*, 13(3-4), 373–384.
- Castro, I. P., Cheng, H., & Reynolds, R. ((2006)). Turbulence over urban-type roughness: Deductions from wind-tunnel measurements. *Boundary-Layer Meteorology*, 118, 109–131.
- Castro, I. P., Xie, Z.-T., Fuka, V., Robins, A. G., Carpentieri, M., Hayden, P., Hertwig, D., & Coceal, O. ((2017)). Measurements and computations of flow in an urban street system. *Boundary-Layer Meteorology*, 162, 207–230.
- Cengiz, C. ((2013)). Urban ecology. In *Advances in landscape architecture*. IntechOpen.
- Cf, O. (2015). Transforming our world: The 2030 agenda for sustainable development. *United Nations: New York, NY, USA*.
- Cheng, H., & Castro, I. P. ((2002)). Near wall flow over urban-like roughness. *Boundary-Layer Meteorology*, 104, 229–259.
- Cheng, W.-C., & Porté-Agel, F. ((2015)). Adjustment of turbulent boundary-layer flow to idealized urban surfaces: A large-eddy simulation study. *Boundary-Layer Meteorology*, 155(2), 249–270.
- Chew, L. W., & Norford, L. K. ((2018)). Pedestrian-level wind speed enhancement in urban street canyons with void decks. *Building and Environment*, 146, 64–76.
- Coceal, O., Dobre, A., & Thomas, T. G. ((2007)). Unsteady dynamics and organized structures from dns over an idealized building canopy. *International Journal of Climatology: A Journal of the Royal Meteorological Society*, 27(14), 1943–1953.
- Coceal, O., Goulart, E. V., Branford, S., Thomas, T. G., & Belcher, S. E. ((2014)). Flow structure and near-field dispersion in arrays of building-like obstacles. *Journal of Wind Engineering and Industrial Aerodynamics*, 125, 52–68.

- Coceal, O., Thomas, T. G., & Belcher, S. E. ((2007)). Spatial variability of flow statistics within regular building arrays. *Boundary-layer meteorology*, 125(3), 537–552.
- Coceal, O., Thomas, T. G., Castro, I. P., & Belcher, S. E. ((2006)). Mean flow and turbulence statistics over groups of urban-like cubical obstacles. *Boundary-Layer Meteorology*, 121, 491–519.
- Comfort, W. ((2006)). Wind danger in the built environment.
- Costa, P. ((2018)). A fft-based finite-difference solver for massively-parallel direct numerical simulations of turbulent flows. *Computers & Mathematics with Applications*, 76(8), 1853–1862.
- Cotella Dalmau, J., Oñate Ibáñez de Navarra, E., & Rossi, R. ((2016)). *Applications of turbulence modeling in civil engineering*. International Centre for Numerical Methods in Engineering (CIMNE).
- Council, N. R., et al. ((2012)). *Assessing the reliability of complex models: Mathematical and statistical foundations of verification, validation, and uncertainty quantification*. National Academies Press.
- Di Sabatino, S., Kastner-Klein, P., Berkowicz, R., Britter, R., & Fedorovich, E. ((2003)). The modelling of turbulence from traffic in urban dispersion models—part i: Theoretical considerations. *Environmental Fluid Mechanics*, 3, 129–143.
- Dimoudi, A., Kantzioura, A., Zoras, S., Pallas, C., & Kosmopoulos, P. ((2013)). Investigation of urban microclimate parameters in an urban center. *Energy and Buildings*, 64, 1–9.
- Dye, R. ((1980)). Comparison of full-scale and wind-tunnel model measurements of ground winds around a tower building. *Journal of Wind Engineering and Industrial Aerodynamics*, 6(3-4), 311–326.
- Fiala, D., et al. ((1998)). *Dynamic simulation of human heat transfer and thermal comfort* [Doctoral dissertation, De Montfort University Leicester, UK].
- Franke, J., Hellsten, A., Schlünzen, H., & Carissimo, B. ((2007)). *Best practice guideline for the cfd simulation of flows in the urban environment* [Doctoral dissertation, COST European Cooperation in Science and Technology].
- García-Sánchez, C., Vitalis, S., Paden, I., & Stoter, J. ((2021)). The impact of level of detail in 3d city models for cfd-based wind flow simulations. *The International Archives of the Photogrammetry, Remote Sensing and Spatial Information Sciences*, 67–72.
- Gunawardena, K. R., Wells, M. J., & Kershaw, T. ((2017)). Utilising green and bluespace to mitigate urban heat island intensity. *Science of the Total Environment*, 584, 1040–1055.
- Henningson, D. S., & Kim, J. ((1991)). On turbulent spots in plane poiseuille flow. *Journal of fluid mechanics*, 228, 183–205.
- Heus, T., van Heerwaarden, C. C., Jonker, H. J., Pier Siebesma, A., Axelsen, S., Van Den Dries, K., Geoffroy, O., Moene, A., Pino, D., De Roode, S., et al. ((2010)). Formulation of the dutch atmospheric large-eddy simulation (dales) and overview of its applications. *Geoscientific Model Development*, 3(2), 415–444.
- HU, Z., & Sandham, N. ((2001)). Dns databases for turbulent couette and poiseuille flow.
- Hui, Y., Yuan, K., Chen, Z., & Yang, Q. ((2019)). Characteristics of aerodynamic forces on high-rise buildings with various façade appurtenances. *Journal of Wind Engineering and Industrial Aerodynamics*, 191, 76–90.
- Hunt, J., Poulton, E., & Mumford, J. ((1976)). The effects of wind on people; new criteria based on wind tunnel experiments. *Building and Environment*, 11(1), 15–28.
- Janssen, W., Blocken, B., & van Hooff, T. ((2013)). Pedestrian wind comfort around buildings: Comparison of wind comfort criteria based on whole-flow field data for a complex case study. *Building and Environment*, 59, 547–562.
- Jian, Z., Fan, Z., Zhonghua, G., & Liu, P. ((2022)). Assessment of macroclimate and microclimate effects on outdoor thermal comfort via artificial neural network models. *Urban Climate*, 42, 101134.
- Jianlin, L., Niu, J., Du, Y., Mak, C. M., & Zhang, Y. ((2019)). Les for pedestrian level wind around an idealized building array—assessment of sensitivity to influencing parameters. *Sustainable Cities and Society*, 44, 406–415.
- Jones, W. P., & Launder, B. E. ((1972)). The prediction of laminarization with a two-equation model of turbulence. *International journal of heat and mass transfer*, 15(2), 301–314.
- Kamei, I., & Maruta, E. ((1979)). Study on wind environmental problems caused around buildings in japan. *Journal of Wind Engineering and Industrial Aerodynamics*, 4(3-4), 307–331.

- Kanda, M., Moriwaki, R., & Kasamatsu, F. ((2004)). Large-eddy simulation of turbulent organized structures within and above explicitly resolved cube arrays. *Boundary-Layer Meteorology*, 112, 343–368.
- Katolický, J., & Jicha, M. ((2005)). Eulerian–lagrangian model for traffic dynamics and its impact on operational ventilation of road tunnels. *Journal of Wind Engineering and Industrial Aerodynamics*, 93(1), 61–77.
- Kenjereš, S., & ter Kuile, B. ((2013)). Modelling and simulations of turbulent flows in urban areas with vegetation. *Journal of Wind Engineering and Industrial Aerodynamics*, 123, 43–55.
- Kim, J., & Moin, P. ((1985)). Application of a fractional-step method to incompressible navier-stokes equations. *Journal of computational physics*, 59(2), 308–323.
- Kim, J., Moin, P., & Moser, R. ((1987)). Turbulence statistics in fully developed channel flow at low reynolds number. *Journal of fluid mechanics*, 177, 133–166.
- Klotz, S. ((1986)). Buchbesprechung] experimentelle landschaftsökologie. lehrbuch der umweltforschung I. auflage, j. barner, stuttgart, ferdinand enke verlag (1983), viii, 196 s., 52 abb., 7 tabellen kartoniert, 39, 80 dm.
- Kluková, Z., Nosek, Š., Fuka, V., Jaňour, Z., Chaloupecká, H., & Ďoubalová, J. ((2021)). The combining effect of the roof shape, roof-height non-uniformity and source position on the pollutant transport between a street canyon and 3d urban array. *Journal of Wind Engineering and Industrial Aerodynamics*, 208, 104468.
- Kong, H., Choi, H., & Lee, J. S. ((2000)). Direct numerical simulation of turbulent thermal boundary layers. *Physics of Fluids*, 12(10), 2555–2568.
- Krüger, E., Minella, F., & Rasia, F. ((2011)). Impact of urban geometry on outdoor thermal comfort and air quality from field measurements in Curitiba, Brazil. *Building and Environment*, 46(3), 621–634.
- Lam, K. M. ((1992)). Wind environment around the base of a tall building with a permeable intermediate floor. *Journal of Wind Engineering and Industrial Aerodynamics*, 2313.
- Lamberti, G., Amerio, L., Pomaranzi, G., Zasso, A., & Gorlé, C. ((2020)). Comparison of high resolution pressure measurements on a high-rise building in a closed and open-section wind tunnel. *Journal of wind engineering and industrial aerodynamics*, 204, 104247.
- Liu, J., Heidarinejad, M., Pitchurov, G., Zhang, L., & Srebric, J. ((2018)). An extensive comparison of modified zero-equation, standard k- ϵ , and LES models in predicting urban airflow. *Sustainable cities and society*, 40, 28–43.
- Liu, S., Pan, W., Zhao, X., Zhang, H., Cheng, X., Long, Z., & Chen, Q. ((2018)). Influence of surrounding buildings on wind flow around a building predicted by CFD simulations. *Building and Environment*, 140, 1–10.
- Lund, T. S., Wu, X., & Squires, K. D. ((1998)). Generation of turbulent inflow data for spatially-developing boundary layer simulations. *Journal of computational physics*, 140(2), 233–258.
- Manley, G. ((1958)). On the frequency of snowfall in metropolitan England. *Quarterly Journal of the Royal Meteorological Society*, 84(359), 70–72.
- Maruyama, T., & Ishizaki, H. ((1988)). A wind tunnel test on the boundary layer characteristics above an urban area. *Journal of Wind Engineering and Industrial Aerodynamics*, 28(1-3), 139–148.
- Melbourne, W. ((1978)). Criteria for environmental wind conditions. *Journal of Wind Engineering and Industrial Aerodynamics*, 3(2-3), 241–249.
- Melbourne, W. H. ((1971)). *Ground level winds caused by large buildings*. Monash University, Department of Mechanical Engineering.
- Mittal, H., Sharma, A., & Gairola, A. ((2018)). A review on the study of urban wind at the pedestrian level around buildings. *Journal of Building Engineering*, 18, 154–163.
- Moin, P., & Mahesh, K. ((1998)). Direct numerical simulation: A tool in turbulence research. *Annual review of fluid mechanics*, 30(1), 539–578.
- Nosek, Š., Fuka, V., Kukačka, L., Kluková, Z., & Jaňour, Z. ((2018)). Street-canyon pollution with respect to urban-array complexity: The role of lateral and mean pollution fluxes. *Building and Environment*, 138, 221–234.
- Palme, M., & Salvati, A. ((2021)). *Urban microclimate modelling for comfort and energy studies*. Springer.
- Penwarden, A. D., & Wise, A. F. E. ((1975)). *Wind environment around buildings*. HM Stationery Office London, UK.

- Peskin, C. S. ((1982)). The fluid dynamics of heart valves: Experimental, theoretical, and computational methods. *Annual review of fluid mechanics*, 14(1), 235–259.
- Pielke Sr, R. A. ((2013)). *Mesoscale meteorological modeling*. Academic press.
- Plate, E. J. ((1999)). Methods of investigating urban wind fields—physical models. *Atmospheric Environment*, 33(24-25), 3981–3989.
- Pope, S. B. ((2001)). Turbulent flows. *Measurement Science and Technology*, 12(11), 2020–2021.
- Pourquie, M., Breugem, W.-P., & Boersma, B. J. ((2009)). Some issues related to the use of immersed boundary methods to represent square obstacles. *International Journal for Multiscale Computational Engineering*, 7(6).
- Rajasekarababu, K., Vinayagamurthy, G., & Selvi Rajan, S. ((2022)). Evaluation of cfd urans turbulence models for the building under environmental wind flow with experimental validation. *Journal of Applied Fluid Mechanics*, 15(5), 1387–1401.
- Raupach, M. R., Antonia, R. A., & Rajagopalan, S. ((1991)). Rough-wall turbulent boundary layers.
- Rhie, C. M., & Chow, W.-L. ((1983)). Numerical study of the turbulent flow past an airfoil with trailing edge separation. *AIAA journal*, 21(11), 1525–1532.
- Ricci, A., & Blocken, B. ((2020)). On the reliability of the 3d steady rans approach in predicting microscale wind conditions in seaport areas: The case of the ijmuiden sea lock. *Journal of Wind Engineering and Industrial Aerodynamics*, 207, 104437.
- Shih, T.-H., Liou, W. W., Shabbir, A., Yang, Z., & Zhu, J. ((1995)). A new $k-\epsilon$ eddy viscosity model for high reynolds number turbulent flows. *Computers & fluids*, 24(3), 227–238.
- Solinas, M., Goldberg, S. R., & Piomelli, D. ((2008)). The endocannabinoid system in brain reward processes. *British journal of pharmacology*, 154(2), 369–383.
- Stathopoulos, T., & Storms, R. ((1986)). Wind environmental conditions in passages between buildings. *Journal of Wind Engineering and Industrial Aerodynamics*, 24(1), 19–31.
- Stoll, R., Gibbs, J. A., Salesky, S. T., Anderson, W., & Calaf, M. ((2020)). Large-eddy simulation of the atmospheric boundary layer. *Boundary-Layer Meteorology*, 177, 541–581.
- Tan, S., & Huang, L. ((2014)). A staggered-grid finite-difference scheme optimized in the time–space domain for modeling scalar-wave propagation in geophysical problems. *Journal of Computational Physics*, 276, 613–634.
- Tomas, J., Eisma, H., Pourquie, M., Elsinga, G., Jonker, H., & Westerweel, J. ((2017)). Pollutant dispersion in boundary layers exposed to rural-to-urban transitions: Varying the spanwise length scale of the roughness. *Boundary-Layer Meteorology*, 163, 225–251.
- Tomas, J., Pourquie, M., & Jonker, H. J. ((2016)). Stable stratification effects on flow and pollutant dispersion in boundary layers entering a generic urban environment. *Boundary-Layer Meteorology*, 159, 221–239.
- Tominaga, Y., Mochida, A., Yoshie, R., Kataoka, H., Nozu, T., Yoshikawa, M., & Shirasawa, T. ((2008)). Aij guidelines for practical applications of cfd to pedestrian wind environment around buildings. *Journal of wind engineering and industrial aerodynamics*, 96(10-11), 1749–1761.
- Toosi, S., & Larsson, J. ((2018)). Grid-adaptation and convergence-verification in large eddy simulation: A robust and systematic approach. *2018 Fluid Dynamics Conference*, 3406.
- Toparlar, Y., Blocken, B., Maiheu, B., & Van Heijst, G. ((2017)). A review on the cfd analysis of urban microclimate. *Renewable and Sustainable Energy Reviews*, 80, 1613–1640.
- Toparlar, Y., Blocken, B., Vos, P. v., Van Heijst, G., Janssen, W., van Hooff, T., Montazeri, H., & Timmermans, H. ((2015)). Cfd simulation and validation of urban microclimate: A case study for bergpolder zuid, rotterdam. *Building and environment*, 83, 79–90.
- Uematsu, Y., Yamada, M., Higashiyama, H., & Orimo, T. ((1992)). Effects of the corner shape of high-rise buildings on the pedestrian-level wind environment with consideration for mean and fluctuating wind speeds. *Journal of Wind Engineering and Industrial Aerodynamics*, 44(1-3), 2289–2300.
- UNDESA, P. ((2018)). World urbanization prospects: The 2018 revision. Retrieved August, 26, 2018.
- Vanky, P., Mark, A., Hunger, F., Haeger-Eugensson, M., Tarraso, J., Adelfio, M., Kalagasidis, A. S., & Sardina, G. ((2023)). Addressing wind comfort in an urban area using an immersed boundary framework. *Technische Mechanik-European Journal of Engineering Mechanics*, 43(1), 151–161.
- Vreman, A. ((2004)). An eddy-viscosity subgrid-scale model for turbulent shear flow: Algebraic theory and applications. *Physics of fluids*, 16(10), 3670–3681.
- Water, F. L. ((2005)). The beaufort wind scale.

- Wesseling, P. ((2009)). *Principles of computational fluid dynamics* (Vol. 29). Springer Science & Business Media.
- Willemsen, E., & Wisse, J. A. ((2007)). Design for wind comfort in the netherlands: Procedures, criteria and open research issues. *Journal of Wind Engineering and Industrial Aerodynamics*, 95(9-11), 1541–1550.
- Yakhot, V., & Orszag, S. A. ((1986)). Renormalization group analysis of turbulence. i. basic theory. *Journal of scientific computing*, 1(1), 3–51.
- Yamada & Koike. ((2011)). Downscaling mesoscale meteorological models for computational wind engineering applications. *Journal of Wind Engineering and Industrial Aerodynamics*, 99(4), 199–216.
- Yamada, M., Uematsu, Y., & Sasaki, R. ((1996)). A visual technique for the evaluation of the pedestrian-level wind environment around buildings by using infrared thermography. *Journal of Wind Engineering and Industrial Aerodynamics*, 65(1-3), 261–271.
- Yamada & Mellor. ((1975)). A simulation of the wangara atmospheric boundary layer data. *Journal of Atmospheric Sciences*, 32(12), 2309–2329.
- Yang, J., & Balaras, E. ((2006)). An embedded-boundary formulation for large-eddy simulation of turbulent flows interacting with moving boundaries. *Journal of computational Physics*, 215(1), 12–40.
- Zhang, X., Tse, K.-T., Weerasuriya, A. U., Li, S., Kwok, K. C., Mak, C. M., Niu, J., & Lin, Z. ((2017)). Evaluation of pedestrian wind comfort near ‘lift-up’ buildings with different aspect ratios and central core modifications. *Building and Environment*, 124, 245–257.
- Zhao, Y., Li, R., Feng, L., Wu, Y., Niu, J., & Gao, N. ((2022)). Boundary layer wind tunnel tests of outdoor airflow field around urban buildings: A review of methods and status. *Renewable and Sustainable Energy Reviews*, 167, 112717.
- Zheng, X., Montazeri, H., & Blocken, B. ((2020)). Cfd simulations of wind flow and mean surface pressure for buildings with balconies: Comparison of rans and les. *Building and Environment*, 173, 106747.
- Zhou, Y., & Hanna, S. R. ((2007)). Along-wind dispersion of puffs released in a built-up urban area. *Boundary-layer meteorology*, 125, 469–486.